Dynamics of patchy vegetation patterns in the two-dimensional generalized Klausmeier model

Tony Wong [*], Michael J. Ward [†]

Abstract

We study the dynamical and steady-state behavior of self-organized spatially localized patches or "spots" of vegetation for the Klausmeier reaction-diffusion (RD) system of spatial ecology that models the interaction between surface water and vegetation biomass on a 2-D spatial landscape with a spatially uniform terrain slope gradient. In this context, we develop and implement a hybrid asymptotic-numerical theory to analyze the existence, linear stability, and slow dynamics of multi-spot quasi-equilibrium spot patterns for the Klausmeier model in the singularly perturbed limit where the biomass diffusivity is much smaller than that of the water resource. From the resulting differential-algebraic (DAE) system of ODEs for the spot locations, one primary focus is to analyze how the constant slope gradient influences the steady-state spot configuration. In the unit square, global bifurcation diagrams for two- and three-spot vertically aligned equilibria of the DAE dynamics are determined in terms of this spatially uniform slope gradient. It is shown that if this gradient exceeds a certain threshold depending on the rainfall rate, the DAE dynamics allows for a linearly stable two-spot vertically aligned steady-state with spots located on the uphill side of the terrain. Our second primary focus is to examine bifurcations in quasi-equilibrium multi-spot patterns that are triggered by a slowly varying time-dependent rainfall rate. In particular, we show that a slowly increasing rainfall rate can trigger self-replication events for the localized vegetation patches, whereas a slowly decreasing rainfall rate can initiate spot-annihilation events leading to fewer patches of vegetation. A detailed analysis of delayed bifurcation behavior for each of these two possible transitions is provided in a simple setting. Many full numerical simulations of the Klausmeier RD system are performed both to illustrate the effect of the terrain slope and rainfall rate on localized spot patterns, as well as to validate the predictions from our hybrid asymptotic-numerical theory.

1 Introduction

Reaction diffusion (RD) systems provide a ubiquitous modeling framework for studying pattern formation phenomena in biology, chemistry and spatial ecology. In recent years, there has been a focus on using RD systems to model spatial patterns of vegetation in semi-arid environments (cf. [16], [17]). Depending on the level of aridity, nontrivial vegetation patterns consisting of either gaps, stripes, or spots, have been observed in nature. Full numerical simulations for various RD systems that model the interaction between biomass and the available water resource have qualitatively reproduced this richness in the pattern forming properties (cf. [25], [16], [8], [28]).

In spatial ecology, the Klausmeier model [10] is a two-component RD system with advection that describes the dynamic interaction between surface water and vegetation biomass in a semi-arid ecosystem on a sloped spatial terrain. In this original Klausmeier model, where there is no diffusion term for the water component, the advection term models the downward flow of water induced by a uniformly sloped spatial terrain. However, since patterned vegetation can also be found on flat terrain, water advection alone is typically not the only mechanism underlying patterns of biomass. As a result, several extended Klausmeier RD models (cf. [18], [19], [24]) have been proposed that include a water diffusion term. With such a regularization, and with a suitable scaling of the parameters, the existence and linear stability of localized 1-D vegetation patterns have been well-studied using geometric singular perturbation theory (cf. [18]). In this 1-D context, it was shown in [3] that spikes can move either uphill or downhill the slope, depending on the convexity of the terrain. Moreover, in [3], criteria for the detection of spike annihilation under a decreasing rainfall rate, for both regularly and irregularly spaced spikes, were derived.

In contrast, in a multi-dimensional context, the analysis of pattern formation for the extended Klausmeier model has been primarily restricted to the study of stripe patterns, which are obtained by extending 1-D spike patterns

[*]Department of Mathematics, University of British Columbia, Vancouver, Canada, V6T 1Z2
[†]Department of Mathematics, University of British Columbia, Vancouver, Canada V6T 1Z2, (corresponding author)

in the transverse direction (cf. [2], [19], [12]). One main result of these studies is that a sufficiently large terrain slope gradient can stabilize a transverse 1-D homoclinic pattern in a rectangular domain, which would otherwise be unstable to breakup into spots without a slope gradient. With regards to spatially localized 2-D spot patterns, in [21] the slow dynamics and self-replication behavior of a one-spot solution to the extended Klausmeier RD system was analyzed on a 2-D manifold, which models an arbitrary topography for the spatial landscape. Inspired by the modeling and computational study of [7], the goal in [21] was to analyze how the dynamics of a spot depends on geometrical features of the landscape, such as its curvature. One key aspect of the study in [21] (see also [20]) was the pioneering use of tools in microlocal analysis and differential geometry that are essential for an efficient numerical calculation of a surface Green's function and its regular part, which are required for the numerical solution of the ODE for slow spot dynamics on an arbitrary landscape.

An important aspect in predicting patterns of biomass is the availability of the water resource, which can be modeled by a time-dependent rainfall rate. In this direction, the transition from a spatially uniform to a sparser vegetation state under a slowly receding rainfall was studied in [5]. This study demonstrated that the decreasing speed and the background noise in the rainfall rate are the key factors for determining whether a spatial uniform vegetated state will lead to patterned state, or to a complete absence of biomass (desertification).

The goal of this paper is to analyze the existence, stability, and slow dynamics of localized multi-spot patterns for the extended Klausmeier model, written in non-dimensional form (cf. [19]) in a bounded 2-D domain Ω as

$$v_t = \varepsilon^2 \Delta v - mv + uv^2 \,, \quad u_t = \Delta u + Hu_x - u + a - \varepsilon^{-2} uv^2 \,, \quad \text{in} \quad \Omega \,; \qquad \partial_b v = \partial_n u = 0 \,, \quad \text{in} \quad \partial\Omega \,. \tag{1.1}$$

In this model, v and u represent the vegetation biomass and surface water, respectively, m is the mortality rate of vegetation, $H > 0$ is the constant terrain slope, and $a > 0$ is the rainfall rate. The small parameter $\varepsilon \ll 1$ accounts for the small diffusivity ratio between the biomass and the water (water diffuses much faster than biomass).

In §2, we use the method of matched asymptotic expansions to construct quasi-equilibrium multi-spot solutions and to derive a differential-algebraic (DAE) system of ODEs that governs the slow dynamics of spots over asymptotically long time scales $t = \mathcal{O}(\varepsilon^{-2})$. The numerical implementation of this DAE system in a rectangular domain relies on the derivation in Appendix A of a novel rapidly converging infinite series representation for a Green's function with a uniform advection term. In §3, we perform a linear stability analysis to study $\mathcal{O}(1)$ time-scale instabilities for these multi-spot quasi-equilibria. We show that a peanut-shaped deformation of a spot is unstable if the rainfall rate exceeds a threshold. This linear instability can trigger a nonlinear spot-splitting event. In contrast, for the class of locally radially symmetric perturbations near the spots, we derive a globally coupled eigenvalue problem (GCEP) that characterizes competition instabilities for multi-spot quasi-equilibria. A numerical winding number algorithm is used to detect unstable eigenvalues for this GCEP. Competition instabilities are $\mathcal{O}(1)$ time-scale linear instabilities of the spot amplitudes, which decrease the amplitude of some spots at the expense of others. As observed from full PDE computations of (1.1), this linear instability typically triggers spot-annihilation events. Although the methodology for the analysis of quasi-equilibrium multi-spot patterns for (1.1) and their linear instabilities is closely related to that used in previous studies for related RD systems with no advection (cf. [13], [4], [27]), our focus will be to highlight new solution features for spot patterns of (1.1) that are due to the terrain slope gradient and a slowly varying rainfall rate.

In §4 we use the DAE dynamics, the linear stability theory, and global bifurcation diagrams of spot equilibria computed from the DAE, to study the effect of the terrain slope gradient on the existence, slow dynamics and linear stability on an $\mathcal{O}(1)$ time-scale of N-spot patterns, with $N \leq 3$, in the unit square. From the criterion in Appendix B, we also study the linear stability of the steady-state spot locations with respect to the DAE dynamics. Unstable eigenvalues of the linearization of the DAE dynamics are weak instabilities, i.e. $\lambda = \mathcal{O}(\varepsilon^2)$, and so are manifested only over long time-scales. For a one-spot steady-state solution we identify the region in the a versus H parameter space where the spot is linearly stable to a peanut-shaped deformation. Moreover, we show that linearly stable vertically aligned two-spot steady-state patterns will occur on the uphill side of the terrain slope when the uniform slope gradient exceeds a threshold. For three-spot patterns, and in a certain parameter regime, it is shown that vertically aligned three-spot steady states are unstable. For this case, the linearly stable pattern consists of two vertically aligned spots on the uphill side of the terrain slope with the remaining spot centered on the domain midline on the downhill side of the slope. Full numerical computations of spot trajectories from the PDE (1.1) are used both to illustrate the effect of the terrain slope on slow spot dynamics and to validate the asymptotic theory.

In §5 we study the effects of a slowly varying time-dependent rainfall rate on the slow dynamics and steady-states for multi-spot quasi-equilibria. In §5.1 we show that a slowly decreasing rainfall rate can lead to the onset of competition instabilities, which trigger spot-annihilation events. By augmenting the DAE system for slow spot dynamics with a zero-eigenvalue crossing condition, which is based on the GCEP from the linear stability theory, we can predict the onset time for a competition instability and, most typically, identify the particular spot that will be annihilated. With this augmented DAE algorithm, which incorporates sudden transitions due to spot-annihilation events, the DAE dynamics can be integrated in time until a final steady-state pattern is obtained. The predictions of the spot trajectories and the coarsening behavior of multi-spot quasi-equilbria, as computed from this DAE algorithm, are shown to agree very favorably with full numerical results computed from the PDE (1.1).

In §5.2 and §5.3 we study delayed bifurcation behavior for spot-annihilation and spot-splitting that occurs for either a slowly decreasing or a slowly increasing rainfall rate, respectively. Although criteria for the delayed onset of instabilities due to slowly varying control parameters have been well-studied for ODE models (cf. [9], [14], [6], [1]), there are relatively much fewer such studies for PDE systems (cf. [22] and the references therein). In particular, in §5.2 we derive from the PDE (1.1) a normal form ODE that describes the delayed transition to spot-annihilation that occurs as the rainfall rate decreases slowly below the saddle-node bifurcation point for the existence of a one-spot steady-state solution for (1.1) in the unit square with $H = 0$. In §5.3 we predict the delayed onset for the peanut-splitting instability that occurs as the rainfall rate increases past the static peanut-splitting threshold. These predictions for the delayed bifurcation behavior are confirmed from full PDE simulations of (1.1). Finally, in §6 we briefly summarize some of our main results and discuss a few problems that warrant further investigation.

2 Quasi-equilibrium spot patterns and slow spot dynamics

In the limit $\varepsilon \to 0$ we construct a quasi-equilibrium solution for (1.1) in a rectangular domain Ω with localized spots centered at $\mathbf{x}_1, \ldots, \mathbf{x}_N$, which are assumed to be well-separated in the sense that $|\mathbf{x}_i - \mathbf{x}_j| = \mathcal{O}(1)$ for $i \neq j$ and $\text{dist}(\mathbf{x}_j, \partial\Omega) = \mathcal{O}(1)$ as $\varepsilon \to 0$, for $j = 1, \ldots, N$. Under the assumption that the spots are linearly stable on $\mathcal{O}(1)$ time intervals, we will derive a differential-algebraic (DAE) ODE system characterizing their slow dynamics.

Near the the j^{th} spot centered at $\mathbf{x} = \mathbf{x}_j$, we introduce the slow time scale $\sigma = \varepsilon^2 t$ and the local coordinates

$$\mathbf{y} = \varepsilon^{-1}\sqrt{m}\,[\mathbf{x} - \mathbf{x}_j(\sigma)]\,, \quad \rho = |\mathbf{y}|\,, \quad v = \sqrt{m}V_j\,, \quad u = \sqrt{m}U_j\,, \tag{2.1}$$

where $V_j = V_j(\mathbf{y}, \sigma)$ and $U_j = V_j(\mathbf{y}, \sigma)$. From (1.1), we obtain in terms of these local coordinates that on $\mathbf{y} \in \mathbb{R}^2$,

$$\begin{aligned} -\frac{\varepsilon}{\sqrt{m}}\dot{\mathbf{x}}_j \cdot \nabla_{\mathbf{y}} V_j &= \Delta_{\mathbf{y}} V_j - V_j + U_j V_j^2\,, \\ -\frac{\varepsilon}{m}\dot{\mathbf{x}}_j \cdot \nabla_{\mathbf{y}} U_j &= \varepsilon^{-2}\left(\Delta_{\mathbf{y}} U_j - U_j V_j^2\right) + \frac{H}{\varepsilon\sqrt{m}}\partial_{y_1} U_j + \frac{a}{m^{3/2}} - \frac{1}{m}U_j\,, \end{aligned} \tag{2.2}$$

where $\dot{\mathbf{x}_j} \equiv d\mathbf{x}_j/d\sigma$, $\mathbf{y} = (y_1, y_2)^T$, while $\nabla_{\mathbf{y}}$ and $\Delta_{\mathbf{y}}$ denote the gradient and the Laplacian in the $\mathbf{y}$ variable. Next, we expand the local variables as

$$V_j = V_{j0}(\rho) + \varepsilon V_{j1}(\mathbf{y}, \sigma) + \cdots\,, \qquad U_j = U_{j0}(\rho) + \varepsilon U_{j1}(\mathbf{y}, \sigma) + \cdots\,. \tag{2.3}$$

Upon substituting (2.3) into (2.2) we obtain, at leading order, the radially symmetric core problem

$$\Delta_\rho V_{j0} - V_{j0} + U_{j0}V_{j0}^2 = 0\,, \quad \Delta_\rho U_{j0} - U_{j0}V_{j0}^2 = 0\,, \quad 0 < \rho < \infty\,, \tag{2.4a}$$

$$V_{j0}'(0) = U_{j0}'(0) = 0\,; \quad V_{j0} \to 0\,, \quad U_{j0} \sim S_j \log\rho + \chi(S_j)\,, \quad \rho \to \infty\,, \tag{2.4b}$$

where $\Delta_\rho \equiv \partial_{\rho\rho} + \rho^{-1}\partial_\rho$. Here, we have imposed a logarithmic growth for U_{j0} as $\rho \to \infty$ defined in terms of an unknown constant, S_j, referred to as the spot source strength. The constant $\chi = \chi(S_j)$ in (2.4b) must be computed numerically from this BVP (see the left panel of Fig. 1a). By integrating the U_{j0} equation in (2.4a) over $0 < \rho < \infty$, we use the divergence theorem to obtain the identity

$$S_j = \int_0^\infty U_{j0}V_{j0}^2\,\rho\,d\rho\,. \tag{2.5}$$

At the next order, we find upon substituting (2.3) into (2.2) that $\mathbf{v}_1 \equiv (V_{j1}, U_{j1})^T$ satisfies

$$\Delta_{\mathbf{y}}\mathbf{v}_1 + \mathcal{M}_0\mathbf{v}_1 = \mathbf{f}_c\cos\theta + \mathbf{f}_s\sin\theta\,, \qquad \mathbf{y} \in \mathbb{R}^2\,, \tag{2.6a}$$

where we write $\mathbf{y} = \rho(\cos\theta, \sin\theta)^T$ and

$$\mathcal{M}_0 \equiv \begin{pmatrix} -1 + 2U_{j0}V_{j0} & V_{j0}^2 \\ -2U_{j0}V_{j0} & -V_{j0}^2 \end{pmatrix}\,, \qquad \mathbf{f}_c \equiv -\frac{1}{\sqrt{m}}\left(V_{j0}'\,\dot{x}_{j1}\,, HU_{j0}'\right)^T\,, \qquad \mathbf{f}_s \equiv -\left(\frac{V_{j0}'\,\dot{x}_{j2}}{\sqrt{m}}\,, 0\right)^T\,. \tag{2.6b}$$

We then decompose $\mathbf{v}_1$ as

$$\mathbf{v}_1 = \mathbf{v}_{1c}\cos\theta + \mathbf{v}_{1s}\sin\theta\,, \tag{2.7a}$$

where $\mathbf{v}_{1c}(\rho) = (V_{1c}, U_{1c})^T$ and $\mathbf{v}_{1s}(\rho) = (V_{1s}, U_{1s})^T$ satisfy

$$\mathcal{L}_1\mathbf{v}_{1c} + \mathcal{M}_0\mathbf{v}_{1c} = \mathbf{f}_c\,, \qquad \mathcal{L}_1\mathbf{v}_{1s} + \mathcal{M}_0\mathbf{v}_{1s} = \mathbf{f}_s\,, \qquad \text{with} \qquad \mathcal{L}_1 \equiv \Delta_\rho - \frac{1}{\rho^2}\,. \tag{2.7b}$$

We can impose that $V_{1c} \to 0$ and $V_{1s} \to 0$ exponentially as $\rho \to \infty$. However, from a simple dominant balance argument, we must seek a far-field behavior for U_{1c} and U_{1s} in the form

$$U_{1c} \sim A_c\,\rho\log\rho + B_c\,\rho\,, \qquad U_{1s} \sim B_s\,\rho\,, \qquad \text{as} \quad \rho\to\infty\,, \tag{2.8}$$

for some coefficients A_c, B_c, and B_s to be found.

To determine these coefficients we proceed as follows. By differentiating the core problem (2.4a) with respect to ρ, we first observe that $\mathbf{v}_h = \left(V_{j0}', U_{j0}'\right)^T$ is a null-vector for the linear operator $\mathcal{L}_1 + \mathcal{M}_0$. Therefore, there is a nontrivial solution $\mathbf{v}_1^\star \equiv (V_1^\star, U_1^\star)^T$ to the homogeneous adjoint problem

$$\mathcal{L}_1\mathbf{v}_1^\star + \mathcal{M}_0^T\mathbf{v}_1^\star = \mathbf{0}\,, \tag{2.9a}$$

for which $V_i^\star \to 0$ exponentially and $U_1^\star = \mathcal{O}(\rho^{-1})$ as $\rho \to \infty$. We normalize this solution by imposing that

$$V_1^\star \to 0\,, \qquad U_1^\star \sim 1/\rho\,, \quad \text{as} \quad \rho \to \infty\,. \tag{2.9b}$$

Next, we invoke a solvability condition for $\mathbf{v}_{1c}$ in (2.7b) that leads to the determination of the values of A_c and B_c. By applying Lagrange's second identity in a large disk $B_R \equiv \{\mathbf{y} : |\mathbf{y}| \le R\}$, we get

$$\int_{B_R} \left[(\mathcal{L}_1\mathbf{v}_{1c} + \mathcal{M}_0\mathbf{v}_{1c})\cdot\mathbf{v}_1^\star - \left(\mathcal{L}_1\mathbf{v}_1^\star + \mathcal{M}_0^T\mathbf{v}_1^\star\right)\cdot\mathbf{v}_{1c}\right] d\mathbf{y} = \int_{\partial B_R} \left(\partial_\rho\mathbf{v}_{1c}\cdot\mathbf{v}_1^\star - \partial_\rho\mathbf{v}_1^\star\cdot\mathbf{v}_{1c}\right) ds\,. \tag{2.10}$$

By using the definitions of $\mathbf{v}_{1c}$ and $\mathbf{v}_1^\star$ in (2.7b) and (2.9a), respectively, we use integration by parts to calculate the left hand side of (2.10) as

$$\begin{aligned}\int_{B_R} \mathbf{f}_c\cdot\mathbf{v}_1^\star\,d\mathbf{y} &= -\frac{2\pi}{\sqrt{m}}\int_0^R \left(V_{j0}'\,V_1^\star\,\dot{x}_{j1} + H\,U_{j0}'\,U_1^\star\right)\,\rho\,d\rho \\ &\sim -\frac{2\pi\dot{x}_{j1}}{\sqrt{m}}\left(\int_0^R V_{j0}'\,V_1^\star\,\rho\,d\rho\right) - \frac{2\pi H}{\sqrt{m}}\left(S_j\log R + \chi(S_j) - \int_0^R U_{j0}\,\left(U_1^\star\rho\right)'\,d\rho\right)\,,\end{aligned} \tag{2.11}$$

as $R \to \infty$. To evaluate the right hand side of (2.10), we use the far-field behavior of U_{1c} and $U_1^\star$ in (2.8) and (2.9b), respectively, to derive for $R \gg 1$ that

$$\begin{aligned}\int_{\partial B_R} \left(\partial_\rho\mathbf{v}_{1c}\cdot\mathbf{v}_1^\star - \partial_\rho\mathbf{v}_1^\star\cdot\mathbf{v}_{1c}\right) ds &\sim 2\pi R\left(U_{1c}'U_1^\star - U_1^{\star\prime}U_{1c}\right)|_{\rho=R}\,, \\ &\sim 2\pi R\left[\left(A_c\log R + A_c + B_c\right)R^{-1} + \left(A_cR\log R + B_cR\right)R^{-2}\right] \\ &\sim 2\pi\left(2A_c\log R + A_c + 2B_c\right)\,.\end{aligned} \tag{2.12}$$

Upon equating the limiting behaviors as $R \to \infty$ in (2.11) and (2.12), we conclude that

$$A_c + 2B_c = -\frac{\dot{x}_{j1}}{\sqrt{m}}\left(\int_0^\infty V_{j0}'V_1^\star\rho\,d\rho\right) - \frac{H}{\sqrt{m}}\left(\chi(S_j) - \int_0^\infty U_{j0}\left(U_1^\star\rho\right)'\,d\rho\right)\,, \qquad 2A_c = -\frac{H}{\sqrt{m}}S_j\,. \tag{2.13}$$

This determines A_c and B_c as

$$A_c = -\frac{HS_j}{2\sqrt{m}}\,, \qquad B_c = \frac{H}{2\sqrt{m}}\left(\frac{S_j}{2} - \chi(S_j) + \int_0^\infty U_{j0}\left(U_1^\star\rho\right)'\,d\rho\right) - \frac{\dot{x}_{j1}}{2\sqrt{m}}\left(\int_0^\infty V_{j0}'V_1^\star\,\rho\,d\rho\right)\,. \tag{2.14a}$$

Similarly, by invoking a solvability condition on the problem (2.7b) for vv_{1s}, we obtain that

$$B_s = -\frac{\dot{x}_{j2}}{2\sqrt{m}}\left(\int_0^\infty V_{j0}'\,V_1^\star\,\rho\,d\rho\right)\,. \tag{2.14b}$$

By combining (2.1), (2.3), (2.4b) and (2.8), and in terms of A_c, B_c, and B_s as given in (2.14), we obtain that the far-field behavior of the inner solution near the j^{th} spot is

$$u = \sqrt{m} U_j \sim \sqrt{m} \left[S_j \log \rho + \chi(S_j) + \varepsilon \left(A_c \, \rho \log \rho + B_c \, \rho \right) \cos \theta + \varepsilon B_s \, \rho \sin \theta \right] \,, \quad \text{as} \quad \rho \to \infty \,. \tag{2.15}$$

Next, we construct the asymptotic solution in the outer region, defined away from $\mathcal{O}(\varepsilon)$ regions near the spots. In the outer region, since v is exponentially small, then $\varepsilon^{-2} uv^2$ is localized near the spots. In the sense of distributions, we use the inner expansion $v = \sqrt{m} V_j$ and $u = \sqrt{m} U_j$, where V_j and U_j are given in (2.3), and the inner variable $|\mathbf{y}| = \varepsilon^{-1} \sqrt{m} |\mathbf{x} - \mathbf{x}_j|$ to calculate for $\varepsilon \to 0$ that

$$\begin{aligned} \varepsilon^{-2} uv^2 &\to \sum_{i=1}^{N} \left[\int_0^{2\pi} \int_0^{\infty} m^{3/2} \left(U_{i0} + \varepsilon U_{i1} + \cdots \right) \left(V_{i0} + \varepsilon V_{i1} + \cdots \right)^2 \frac{\rho}{m} d\rho \, d\theta \right] \delta(\mathbf{x} - \mathbf{x}_i) \,, \\ &= 2\pi \sqrt{m} \sum_{i=1}^{N} \left[S_i + \mathcal{O}(\varepsilon^2) \right] \delta(\mathbf{x} - \mathbf{x}_i) \,. \end{aligned} \tag{2.16}$$

Here, in obtaining the $\mathcal{O}(\varepsilon^2)$ estimate, we used the fact that an integral of V_{1j} or U_{1j} when multiplied by a radially symmetric function must vanish. In this way, upon using (2.16) the outer problem for u to the order of $\mathcal{O}(\varepsilon^2)$ is

$$\Delta u + H u_x - u = -a + 2\pi \sqrt{m} \sum_{i=1}^{N} S_i \, \delta(\mathbf{x} - \mathbf{x}_i) \,, \quad \text{in } \Omega \,; \qquad \partial_n u = 0 \,, \quad \text{on } \partial\Omega \,. \tag{2.17}$$

We will represent the solution to (2.17) in terms of the Green's function $G(\mathbf{x}; \mathbf{z})$ satisfying

$$\Delta G + H G_x - G = -\delta(\mathbf{x} - \mathbf{z}) \,, \quad \text{in } \Omega \,; \qquad \partial_n G = 0 \quad \text{on } \partial\Omega \,, \tag{2.18}$$

where $\mathbf{x} = (x, y)^T$ and $\mathbf{z} = (z_1, z_2)^T$. To eliminate the gradient term in (2.18) we introduce $F(\mathbf{x}; \mathbf{z})$ by

$$G(\mathbf{x}; \mathbf{z}) \equiv e^{K(z_1 - x)} F(\mathbf{x}; \mathbf{z}) \,, \qquad \text{where} \qquad K \equiv H/2 \,. \tag{2.19}$$

In the rectangular domain $\Omega = \{(x, y) \, | \, 0 < x < l \,, \, 0 < y < h\}$, we obtain that $F(\mathbf{x}; \mathbf{z})$ is the solution to

$$\Delta F - (1 + K^2) F = -\delta(\mathbf{x} - \mathbf{z}) \quad \text{in } \Omega \,, \tag{2.20a}$$

$$F_x - K F = 0 \,, \quad \text{on } x = 0, l \,; \qquad F_y = 0 \,, \quad \text{on } y = 0, h \,, \tag{2.20b}$$

$$F = -\frac{1}{2\pi} \log |\mathbf{x} - \mathbf{z}| + R(\mathbf{z}; \mathbf{z}) + o(1) \,, \quad \text{as} \quad \mathbf{x} \to \mathbf{z} \,, \tag{2.20c}$$

where $R(\mathbf{z}; \mathbf{z})$ is the regular part of the Green's function.

In terms of this Green's function in (2.19), the outer solution satisfying (2.17) is

$$u(\mathbf{x}) = a - 2\pi \sqrt{m} \sum_{i=1}^{N} S_i \, G(\mathbf{x}; \mathbf{x}_i) = a - 2\pi \sqrt{m} \sum_{i=1}^{N} S_i \, e^{K(x_i - x)} F(\mathbf{x}; \mathbf{x}_i) \,, \tag{2.21}$$

where $\mathbf{x}_i = (x_i, y_i)^T$ is the center of the i^{th} spot. Next, we expand u as $\mathbf{x} \to \mathbf{x}_j$ by using the local behavior of $G(\mathbf{x}; \mathbf{x}_j)$ as $\mathbf{x} \to \mathbf{x}_j$, together with a Taylor-expansion of the remaining terms. For $\mathbf{x} \to \mathbf{x}_j$, we obtain that

$$\begin{aligned} u \sim a &- 2\pi \sqrt{m} \left(S_j R_{jj} + \sum_{i \neq j}^{N} S_i \, e^{K(x_i - x_j)} F_{j,i} \right) + \sqrt{m} S_j \log |\mathbf{x} - \mathbf{x}_j| - \sqrt{m} S_j K (x - x_j) \log |\mathbf{x} - \mathbf{x}_j| \\ &- 2\pi \sqrt{m} \left[S_j \left(-K \mathbf{e}_1 R_{j,j} + \nabla_{\mathbf{x}} R_{j,j} \right) + \sum_{i \neq j}^{N} S_i e^{K(x_i - x_j)} \left(-K \mathbf{e}_1 F_{j,i} + \nabla_{\mathbf{x}} F_{j,i} \right) \right] \cdot (\mathbf{x} - \mathbf{x}_j) \\ &+ \mathcal{O} \left(|\mathbf{x} - \mathbf{x}_j|^2 \log |\mathbf{x} - \mathbf{x}_j| \right) \,, \end{aligned} \tag{2.22}$$

where $\mathbf{x} = (x,y)^T$. Here $\mathbf{e}_1 \equiv (1,0)^T$, $F_{j,i} \equiv F(\mathbf{x}_j;\mathbf{x}_i)$, $\nabla_{\mathbf{x}} F_{j,i} \equiv \nabla_{\mathbf{x}} F(\mathbf{x};\mathbf{x}_i)|_{\mathbf{x}=\mathbf{x}_j}$, $R_{j,j} \equiv R(\mathbf{x}_j;\mathbf{x}_j)$, and $\nabla_{\mathbf{x}} R_{j,j} \equiv \nabla_{\mathbf{x}} R(\mathbf{x};\mathbf{x}_j)|_{\mathbf{x}=\mathbf{x}_j}$. In terms of the inner variable $\mathbf{y} = \varepsilon^{-1}\sqrt{m}(\mathbf{x}-\mathbf{x}_j)$ we obtain from (2.22) that

$$\begin{aligned} u \sim a + \sqrt{m}\, S_j \log\left(\frac{\varepsilon\rho}{\sqrt{m}}\right) - 2\pi\sqrt{m}\left(S_j R_{j,j} + \sum_{i\neq j}^{N} S_i\, e^{K(x_i-x_j)}\, F_{j,i}\right) - \varepsilon K S_j \log\left(\frac{\varepsilon\rho}{\sqrt{m}}\right)\rho\cos\theta \\ - 2\pi\varepsilon\left[S_j\left(-K R_{j,j}\mathbf{e}_1 + \nabla_{\mathbf{x}} R_{j,j}\right) + \sum_{i\neq j}^{N} S_i\, e^{K(x_i-x_j)}\,\left(-K F_{j,i}\mathbf{e}_1 + \nabla_{\mathbf{x}} F_{j,i}\right)\right]\cdot\mathbf{y} + \mathcal{O}(\varepsilon^2\log\varepsilon)\,, \end{aligned} \tag{2.23}$$

where we recall that $K \equiv H/2$ and $\mathbf{e}_1 \equiv (1,0)^T$.

We now match (2.15) and (2.23). At the leading order, and upon defining $\nu \equiv -1/\log\varepsilon$, we have

$$\left(1 + \frac{\nu\log m}{2}\right) S_j + 2\pi\nu\left(S_j R_{j,j} + \sum_{i\neq j}^{N} S_i\, e^{K(x_i-x_j)} F_{j,i}\right) + \nu\chi(S_j) = \frac{\nu a}{\sqrt{m}}\,, \quad j = 1,\ldots,N\,. \tag{2.24}$$

To write (2.24) in matrix form we let $\mathcal{G} \in \mathbb{R}^{N\times N}$ be the Green's matrix of $\mathbf{x}_1,\ldots,\mathbf{x}_N$, with matrix entries

$$(\mathcal{G})_{i,j} = \begin{cases} R_{j,j} & \text{if } i = j\,, \\ e^{K(x_j-x_i)}\, F_{i,j} & \text{if } i \neq j\,. \end{cases} \tag{2.25}$$

Upon defining $\mathbf{s} \equiv (S_1,\ldots,S_N)^T$, $\boldsymbol{\chi} \equiv (\chi(S_1),\ldots,\chi(S_N))^T$ and $\mathbf{e} \equiv (1,\ldots,1)^T \in \mathbb{R}^N$, we can write (2.24) as the nonlinear algebraic system (NAS)

$$\left(1 + \frac{\nu\log m}{2}\right)\mathbf{s} + 2\pi\nu\,\mathcal{G}\mathbf{s} + \nu\boldsymbol{\chi} = \frac{\nu a}{\sqrt{m}}\,\mathbf{e}\,. \tag{2.26}$$

Next, we match (2.15) and (2.23) at higher order. To do so, we equate the coefficients of $\rho\cos\theta$ and $\rho\sin\theta$ to obtain, respectively, that

$$\begin{aligned} \sqrt{m}\,(A_c\log\rho + B_c) &\sim -K S_j \log\left(\frac{\varepsilon\rho}{\sqrt{m}}\right) - 2\pi\left[S_j\left(-K R_{j,j} + \partial_x R_{j,j}\right) + \sum_{i\neq j}^{N} S_i\, e^{K(x_i-x_j)}\,\left(-K F_{j,i} + \partial_x F_{j,i}\right)\right]\,, \\ \sqrt{m} B_s &\sim -2\pi\left(S_j\partial_y R_{j,j} + \sum_{i\neq j}^{N} S_i\, e^{K(x_i-x_j)}\,\partial_y F_{j,i}\right)\,. \end{aligned} \tag{2.27}$$

Upon substituting (2.14) for A_c, B_c, and B_s directly in (2.27), we solve for $\dot{\mathbf{x}}_j$ to obtain, after some algebra, that

$$\begin{aligned} \dot{\mathbf{x}}_j = \gamma(S_j)\Bigg\{ & K\left[\frac{S_j}{\nu} + \frac{S_j\log m}{2} + \chi(S_j) - \frac{S_j}{2} - \mu(S_j)\right]\mathbf{e}_1 \\ & - 2\pi\left[-K\left(S_j R_{j,j} + \sum_{i\neq j}^{N} S_i e^{K(x_i-x_j)} F_{j,i}\right)\mathbf{e}_1 + S_j\nabla_{\mathbf{x}} R_{j,j} + \sum_{i\neq j}^{N} S_i e^{K(x_i-x_j)}\nabla_{\mathbf{x}} F_{j,i}\right]\Bigg\}, \quad j = 1,\ldots,N\,, \end{aligned} \tag{2.28}$$

where $K = H/2$, and where we have defined $\gamma(S_j)$ and $\mu(S_j)$ by

$$\gamma(S_j) \equiv -\frac{2}{\int_0^\infty V_{j0}'\, V_1^\star\,\rho\, d\rho} \qquad \text{and} \qquad \mu(S_j) \equiv \int_0^\infty U_{j0}\,(\rho\, U_1^\star)'\; d\rho\,. \tag{2.29}$$

In Fig. 1b and Fig. 1c we plot the numerically-computed γ and μ versus S_j, respectively.

Finally, we can further simplify (2.28) by using the NAS (2.24) for the source strengths. In this way, we obtain that the DAE-ODE system governing slow spot dynamics is

$$\frac{d\mathbf{x}_j}{d\sigma} = \gamma(S_j)\left\{K\left[\frac{a}{\sqrt{m}} - \frac{S_j}{2} - \mu(S_j)\right]\mathbf{e}_1 - 2\pi\left(S_j\nabla_{\mathbf{x}} R_{j,j} + \sum_{i\neq j}^{N} S_i e^{K(x_i-x_j)}\nabla_{\mathbf{x}} F_{j,i}\right)\right\}\,, \quad j = 1,\ldots,N\,, \tag{2.30}$$

where $\sigma = \varepsilon^2 t$ and $K = H/2$. Here S_j, for $j = 1, \ldots, N$, are coupled to the spot locations through the NAS (2.24), or equivalently (2.26). The DAE-ODE system (2.30) and (2.24) characterizes slow spot dynamics in the absence of any $\mathcal{O}(1)$ time-scale instability of the spot amplitudes. These instabilities are analyzed in the next section.

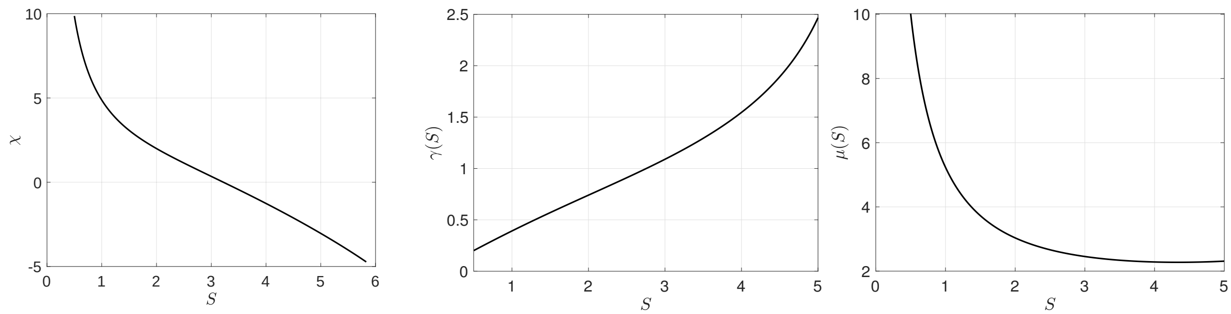

(a) $\chi(S)$ **(b)** $\gamma(S)$ **(c)** $\mu(S)$

Figure 1: Numerical results for $\chi(S)$, $\gamma(S)$, and $\mu(S)$, as defined in (2.4b) and (2.29), as computed numerically from the core problem (2.4a) and the homogeneous adjoint problem (2.9).

3 Linear stability analysis

In this section we study the linear stability on an $\mathcal{O}(1)$ time-scale of the quasi-equilibrium solution, labeled by v_e and u_e, which was constructed in §2. By introducing the perturbation

$$v = v_e + e^{\lambda t}\phi\,, \qquad u = u_e + e^{\lambda t}\eta\,, \tag{3.1}$$

into (1.1), and linearizing, we obtain the following eigenvalue problem with $\partial_n \phi = \partial_n \eta = 0$ on $\partial\Omega$:

$$\varepsilon^2 \Delta\phi - m\phi + 2u_e v_e \phi + v_e^2 \eta = \lambda\phi\,, \qquad \Delta\eta + H\partial_x \eta - \eta - \varepsilon^{-2}\left(2u_e v_e \phi + v_e^2 \eta\right) = \lambda\eta\,, \quad \text{in} \quad \Omega\,. \tag{3.2}$$

There are two distinct types of instabilities for localized spot patterns: instabilities associated with locally non-radially symmetric deformation of a spot, which trigger spot self-replication events [26], and instabilities in the spot amplitudes due to locally radially symmetric perturbations of the spot profile, which can trigger spot-annihilation events (cf. [13], [4], [27], [20], [26]).

To analyze the linear stability of the j^{th} spot centered at $\mathbf{x}_j$, we introduce the local variables Φ_j and N_j by

$$\phi \sim e^{ik\theta}\Phi_j(\rho)\,, \qquad \eta \sim e^{ik\theta} N_j(\rho)\,, \qquad \text{where} \quad \mathbf{y} = \varepsilon^{-1}\sqrt{m}\,(\mathbf{x} - \mathbf{x}_j) = \rho\,(\cos\theta, \sin\theta)^T\,, \tag{3.3}$$

where the integer $k \geq 0$ is the local angular mode. Then, since $v_e \sim \sqrt{m}\,V_{j0}$ and $u_e \sim \sqrt{m}\,U_{j0}$ near the j^{th} spot (see (2.1)), we obtain from (3.2) the following leading-order problem in the inner region, defined on $0 \leq \rho < \infty$:

$$\Delta_\rho \Phi_j - \frac{k^2}{\rho^2}\,\Phi_j - \Phi_j + 2\,U_{j0}V_{j0}\,\Phi_j + V_{j0}^2\,N_j = \frac{\lambda}{m}\,\Phi_j\,, \qquad \Delta_\rho N_j - \frac{k^2}{\rho^2}\,N_j - 2\,U_{j0}V_{j0}\,\Phi_j - V_{j0}^2\,N_j = 0\,. \tag{3.4}$$

We first consider non-radially symmetric perturbations of the spot profile, corresponding to the modes $k > 0$. In particular, the mode $k = 1$ is the translation mode $(\Phi_j, N_j)^T = (U_{j0}', V_{j0}')^T$, which is associated with the neutral eigenvalue $\lambda = 0$. For the modes $k \geq 2$, we can impose $\Phi_j \to 0$ exponentially as $\rho \to \infty$, and that $N_j \sim \mathcal{O}(\rho^{-k})$ as $\rho \to \infty$. In this way, owing to the far-field decay of the inner solution, instabilities for the non-radially symmetric modes are localized near the core of a spot. Since the inner problem (3.4) is the same as for the Schnakenberg RD model studied in [13], the results in [13] for non-radially symmetric instabilities of a localized spot apply to our Klausmeier model. The numerical computation of the eigenvalue $\lambda_{\max}/m$ with the largest real part is given in Fig. 4 of [13] for a range of S_j. For each mode $k \geq 2$, it was found that $\lambda_{\max}$ is real, and $\lambda_{\max}$ is negative (positive) when $S_j < \Sigma_k$ ($S_j > \Sigma_k$). Therefore, the threshold Σ_k (for $k \geq 2$) serves as the largest value of the source strength S_j for which the j^{th} spot is linearly stable to a shape-deforming instability of angular mode k. Moreover, it was shown numerically in [13] that there is an ordering principle $\Sigma_2 < \Sigma_3 < \Sigma_4 < \ldots$ for the instability thresholds, and that $\Sigma_2 \approx 4.302$. In this way, we conclude that an N-spot quasi-equilibrium pattern is linearly stable to local spot-shape deformations if and only if $S_j < \Sigma_2$ for $j = 1, 2, \ldots, N$. Here, $S_1, \ldots, S_N$ are determined in terms of the instantaneous spot locations $\mathbf{x}_1, \ldots, \mathbf{x}_N$ by the NAS (2.26) that applies to our extended Klausmeier model (1.1). The mode $k = 2$, referred to as to the peanut-splitting mode, is the first angular mode to lose stability when S_j is increased. More recently, the weakly nonlinear analysis in [26] for the related Schnakenberg model showed that as the spot source strength exceeds $\Sigma_2 \approx 4.302$, a subcritical pitchfork bifurcation triggers a nonlinear spot-replication event for a steady-state one-spot solution.

The analysis of instabilities associated with locally radially symmetric perturbations, for which $k = 0$, is more intricate since we can no longer impose that $N_j \to 0$ as $\rho \to \infty$. As a result, this instability can only be analyzed through a global coupling of all the local problems near the spots. For $k = 0$, (3.4) yields that

$$\Delta_\rho \Phi_j - \Phi_j + 2U_{j0}V_{j0}\Phi_j + V_{j0}^2 N_j = \frac{\lambda}{m}\Phi_j \,, \qquad \Delta_\rho N_j - 2U_{j0}V_{j0}\Phi_j - V_{j0}^2 N_j = 0 \,. \tag{3.5a}$$

We impose that $\Phi_j \to 0$ exponentially as $\rho \to \infty$, while we must impose that N_j has logarithmic growth, i.e.

$$N_j \sim c_j \left(\log \rho + \hat{B}(S_j; \lambda) \right) \,, \quad \text{as} \quad \rho \to \infty \,. \tag{3.5b}$$

The constant $\hat{B} = \hat{B}(S_j; \lambda)$, depending on S_j and the eigenvalue λ, must be computed from the solution to (3.5). Upon applying the divergence theorem to the N_j equation in (3.5a), we obtain the identify

$$\int_{\mathbb{R}^2} \left(2U_{j0}V_{j0}\Phi_j + V_{j0}^2 N_j \right) \, d\mathbf{y} = 2\pi c_j \,. \tag{3.6}$$

From our analysis of the outer region, we will derive a homogeneous matrix system for the constants $c_1, \ldots, c_N$. This system will have a non-trivial solution only for certain values of λ, which approximate as $\varepsilon \to 0$ the discrete eigenvalues of the linearization (3.1).

In the outer region, ϕ is exponentially small and by using (3.6), we derive in the sense of distributions that

$$\varepsilon^{-2} \left(2u_e v_e \phi + v_e^2 \eta \right) \to \sum_{i=1}^{N} \left[\int_{\mathbb{R}^2} \left(2U_{i0}V_{i0}\Phi_i + V_{i0}^2 N_i \right) \, d\mathbf{y} \right] \delta(\mathbf{x} - \mathbf{x}_i) = 2\pi \sum_{i=1}^{N} c_i \, \delta(\mathbf{x} - \mathbf{x}_i) \,. \tag{3.7}$$

With (3.7), we conclude that the outer problem for η in (3.2) is

$$\Delta \eta + H \partial_x \eta - (1 + \lambda)\eta = 2\pi \sum_{i=1}^{N} c_i \, \delta(\mathbf{x} - \mathbf{x}_i) \,, \quad \text{in} \quad \Omega \,; \quad \partial_n \eta = 0 \quad \text{on} \quad \partial\Omega \,. \tag{3.8}$$

To represent the solution to (3.8) we define the eigenvalue-dependent Green's function $G_\lambda(\mathbf{x}; \mathbf{z})$ by

$$\begin{aligned} &\Delta G_\lambda + H \partial_x G_\lambda - (1 + \lambda) G_\lambda = -\delta(\mathbf{x} - \mathbf{z}) \quad \text{in} \quad \Omega \,, \quad \partial_n G_\lambda = 0 \quad \text{on} \quad \partial\Omega \,, \\ &G_\lambda = -\frac{1}{2\pi} \log |\mathbf{x} - \mathbf{z}| + R_\lambda(\mathbf{z}; \mathbf{z}) + o(1) \,, \quad \text{as} \quad \mathbf{x} \to \mathbf{z} \,. \end{aligned} \tag{3.9}$$

By using the transformation $G_\lambda(\mathbf{x}; \mathbf{z}) = e^{K(z_i - x_i)} F_\lambda(\mathbf{x}; \mathbf{z})$, we obtain in the rectangular domain Ω that F_λ satisfies

$$\Delta F_\lambda - (1 + \lambda + K^2) F_\lambda = -\delta(\mathbf{x} - \mathbf{z}) \quad \text{in} \quad \Omega \,, \tag{3.10a}$$

$$\partial_x F_\lambda - K F_\lambda = 0 \quad \text{on} \quad x = 0, l \,; \qquad \partial_y F_\lambda = 0 \quad \text{on} \quad y = 0, h \,. \tag{3.10b}$$

In Appendix A we show how to numerically calculate F_λ and the regular part $R_\lambda(\mathbf{z}; \mathbf{z})$ efficiently from a rapidly converging infinite series representation. In terms of this Green's function, we represent η in (3.8) as

$$\eta = -2\pi \sum_{i=1}^{N} c_i \, G_\lambda(\mathbf{x}; \mathbf{x}_i) = -2\pi \sum_{i=1}^{N} c_i \, e^{K(x_i - x)} F_\lambda(\mathbf{x}; \mathbf{x}_i) \,, \quad \text{where} \quad K = H/2 \,. \tag{3.11}$$

Next, we match the far-field behavior of the inner solution N_j with the behavior of the outer solution η as $\mathbf{x} \to \mathbf{x}_j$. From (3.11) we calculate as

$$\eta \sim c_j \log|\mathbf{x} - \mathbf{x}_j| - 2\pi \left(c_j R_\lambda(\mathbf{x}_j;\mathbf{x}_j) + \sum_{i \neq j}^{N} c_i \, e^{K(x_i - x_j)} F_\lambda(\mathbf{x}_j;\mathbf{x}_i) \right) + o(1) \,, \tag{3.12}$$

as $\mathbf{x} \to \mathbf{x}_j$. Upon matching (3.5b) with (3.12), we obtain the homogeneous linear system

$$c_j + 2\pi\nu \left(c_j R_\lambda(\mathbf{x}_j;\mathbf{x}_j) + \sum_{i \neq j}^{N} c_i \, e^{K(x_i - x_j)} F_\lambda(\mathbf{x}_j;\mathbf{x}_i) \right) + \nu c_j \hat{B}(S_j;\lambda) = 0 \,, \qquad j = 1, \ldots, N \,. \tag{3.13}$$

For $\lambda \in \mathbb{C}$, we define $\mathbf{c} \equiv (c_1, \ldots, c_N)^T$, the eigenvalue-dependent Green's matrix $\mathcal{G}_\lambda \in \mathbb{C}^{N\times N}$, and the diagonal matrix $\hat{\mathcal{B}} \in \mathbb{C}^{N\times N}$ by

$$[\mathcal{G}_\lambda]_{i,j} = \begin{cases} R_\lambda(\mathbf{x}_j;\mathbf{x}_j) \,, & \text{if} \quad i = j \,, \\ e^{K(x_j - x_i)} F_\lambda(\mathbf{x}_i;\mathbf{x}_j) \,, & \text{if} \quad i \neq j \,. \end{cases} \,, \qquad [\mathcal{B}]_{i,j} = \begin{cases} \hat{B}(S_j;\lambda) \,, & \text{if} \quad i = j \,, \\ 0 \,, & \text{if} \quad i \neq j \,, \end{cases} \tag{3.14}$$

so that we can write (3.13) in matrix form as

$$\mathcal{M}(\lambda)\mathbf{c} = \mathbf{0} \,, \qquad \text{where} \qquad \mathcal{M}(\lambda) \equiv \mathcal{I} + 2\pi\nu\, \mathcal{G}_\lambda + \nu \hat{\mathcal{B}} \,. \tag{3.15a}$$

We refer to the homogeneous linear system (3.15a) for $\mathbf{c}$ as the globally coupled eigenvalue problem (GCEP). This GCEP has a nontrivial solution if and only if

$$\det \mathcal{M}(\lambda) = 0 \,. \tag{3.15b}$$

The values of λ satisfying (3.15b) approximate, as $\varepsilon \to 0$, the discrete eigenvalues of the linearization of the quasi-equilibrium solution for a fixed spatial configuration $\mathbf{x}_1, \ldots, \mathbf{x}_N$ of spots.

The existence of a discrete root λ to (3.15b) satisfying $\text{Re}(\lambda) > 0$ corresponds to a locally radially symmetric instability of the quasi-equilibrium spot pattern. The perturbation of the spot amplitudes are characterized by the corresponding eigenvector $\mathbf{c}$ in (3.15a). To count the number $\mathcal{N}$ of roots of $\det \mathcal{M} = 0$ in the right half of the spectral plane $\text{Re}(\lambda) > 0$, we implement a numerical winding number algorithm based on (3.15b). In our numerical winding number implementation, we use a contour $\mathcal{C}(R, r)$ consisting of semi-circles $\{|\lambda| = R > 0\}$ and $\{|\lambda| = \delta \ll 1\}$ for $-\pi/2 \leq \arg \lambda \leq \pi/2$, which are connected by the imaginary segment $\{\lambda = i\lambda_I : \lambda_I \in \mathbb{R}, \ \delta \leq |\lambda_I| \leq R\}$. From the argument principle of complex analysis, we have

$$\mathcal{N} = \mathcal{P} + \frac{1}{2\pi} \lim_{R\to\infty,\, r\to 0} [\arg \mathcal{F}(\lambda)]_{\mathcal{C}(R,r)} \,, \qquad \text{where} \quad \mathcal{F}(\lambda) \equiv \det \mathcal{M}(\lambda) \,, \tag{3.16}$$

and where $[\arg \mathcal{F}(\lambda)]_{\mathcal{C}(R,r)}$ indicates the change in the argument of $\mathcal{F}(\lambda)$ over the contour. Here, $\mathcal{P}$ is the number of poles of $\det \mathcal{M}(\lambda)$ in the right half of the spectral plane. Since $\mathcal{G}$ is analytic in $\text{Re}(\lambda) > 0$, a pole for $\det \mathcal{M}(\lambda)$ can only arise from the diagonal matrix $\mathcal{B}$. However, from a numerical computation of the inner problem (3.5), we find that $\mathcal{B}$ is analytic in $\text{Re}(\lambda) > 0$ and so $\mathcal{P} = 0$ in (3.16). To determine $\mathcal{N}$, we numerically compute the change of the argument of $\det \mathcal{M}(\lambda)$ over the contour $\mathcal{C}(R, r)$. In our implementation, we took $R = 5$ and $\delta = 10^{-3}$. The results given below were the same for $R > 5$ or for $\delta < 10^{-3}$.

When Ω is the unit square, we now illustrate how a competition instability, leading to spot annihilation, is triggered due to an insufficient rainfall rate a. We take $\varepsilon = 0.02$, $m = 1$ and $H = 0.5$, and we consider two spots that are centered at $(0.7, 0.25)^T$ and $(0.7, 0.75)^T$, respectively. We consider the two choices, $a = 20$ and $a = 30$. Using the winding number criterion (3.16), we obtain there is one root to the GCEP (3.15b) in $\text{Re}(\lambda) > 0$ when $a = 20$, while there are no such roots when $a = 30$. Therefore, we predict that when $a = 20$ ($a = 30$) the two-spot quasi-equilibrium pattern is linearly unstable (stable) to locally radially-symmetric perturbations in the spot amplitudes. The full numerical results from the PDE system (1.1) confirm this prediction from the linear stability theory ,and shows that the competition instability triggers the annihilation of one of the two spots.

In order to detect the emergence of instabilities as parameters are varied, we observe that when $\lambda = 0$ the matrix $\mathcal{M}$ in (3.15a) is reduced to

$$\mathcal{M}_0 = \mathcal{I} + 2\pi\nu\mathcal{G} + \nu\hat{\mathcal{B}}_0 \,, \tag{3.17}$$

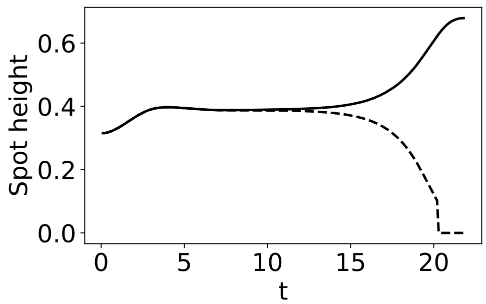

(a) $a = 20$

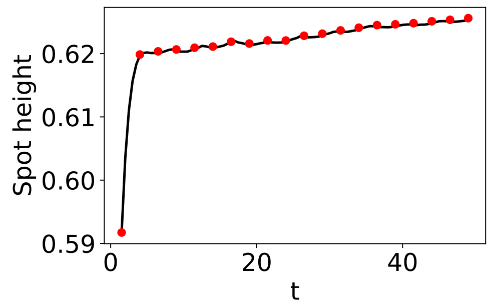

(b) $a = 30$

Figure 2: Full PDE results computed from (1.1) for a two-spot quasi-equilibrium pattern in the unit square for $\varepsilon = 0.02$, $m = 1$ and $H = 0.5$. The spots are centered at $(0.7, 0.25)^T$ and $(0.7, 0.75)^T$. Left panel: For the rainfall rate $a = 20$, the amplitudes of the two spots, as represented by the solid and dashed lines, show a nonlinear spot-annihilation event. Right panel: For $a = 30$, a solid line and red dots are used to represent the two, nearly indistinguishable, spot amplitudes.

where $\mathcal{G}$ is the Green's matrix defined in (2.25), while $\hat{\mathcal{B}}_0 \in \mathbb{R}^{N\times N}$ is defined by

$$\left[\hat{\mathcal{B}}_0\right]_{i,j} = \begin{cases} \chi'(S_j)\,, & \text{if} \quad i = j\,, \\ 0\,, & \text{if} \quad i \neq j\,. \end{cases} \tag{3.18}$$

This result for $\hat{\mathcal{B}}_0$ follows since we can identify that $\hat{B}(S_j; 0) = \chi'(S_j)$ owing to the fact that the solution to (3.5) is $\Phi_j = c_j \partial_S V_{j0}$ and $N_j = c_j \partial_S U_{j0}$ when $\lambda = 0$. The criterion for a zero-eigenvalue crossing for the GCEP is that

$$\det \mathcal{M}_0 = 0\,. \tag{3.19}$$

4 Self-organization of spots

In this section, we fix $m = 1$ and we illustrate the effect of the uniform slope gradient H on the dynamics and linear stability of quasi-equilibrium spot patterns with a small number of spots.

4.1 One-spot patterns

We consider a one-spot pattern in the unit square. By symmetry, the steady-state spot location is always on the midline $y = 1/2$. Therefore, we will focus on the slow dynamics of the one-spot pattern, centered at $\mathbf{x}_1 = (x_1, 1/2)^T$, on this midline. From (2.26), the source strength S_1 for this single spot satisfies the nonlinear scalar equation

$$S_1 + 2\pi\nu S_1 R(\mathbf{x}_1; \mathbf{x}_1) + \nu\chi(S_1) = \nu a\,. \tag{4.1a}$$

For a fixed rainfall rate a, S_1 depends on the spot location as well as the slope gradient through the regular part $R(\mathbf{x}_1; \mathbf{x}_1)$ of the Green's function. In Fig. 3a, we plot S_1 versus x_1 for various values of H when $a = 36$. Upon substituting $N = 1$ into (2.30), the slow spot dynamics is given by the ODE

$$\dot{\mathbf{x}}_1 = \gamma(S_1)\left[K\Big(a - S_1/2 - \mu(S_1)\Big) - 2\pi S_1 \nabla_{\mathbf{x}} R(\mathbf{x}_1; \mathbf{x}_1)\right]\,, \qquad \text{with} \quad K = H/2\,, \tag{4.1b}$$

subject to the algebraic constraint (4.1a). We set $a = 32$ and choose the initial position of the spot to be $\mathbf{x}_1 = (0.4, 1/2)^T$. In Fig. 3b, we compare the spot dynamics computed from the full PDE (1.1) and from the DAE (4.1) for various values of H. From this figure we conclude that the DAE system (4.1) provides a very accurate prediction of the spot trajectory in the absence of any linear instabilities of the pattern.

As discussed in §3, the magnitude of the source strength S_1 gives a prediction for the linear stability of the one-spot pattern to local shape-deforming perturbations. However, we now illustrate through a full PDE numerical

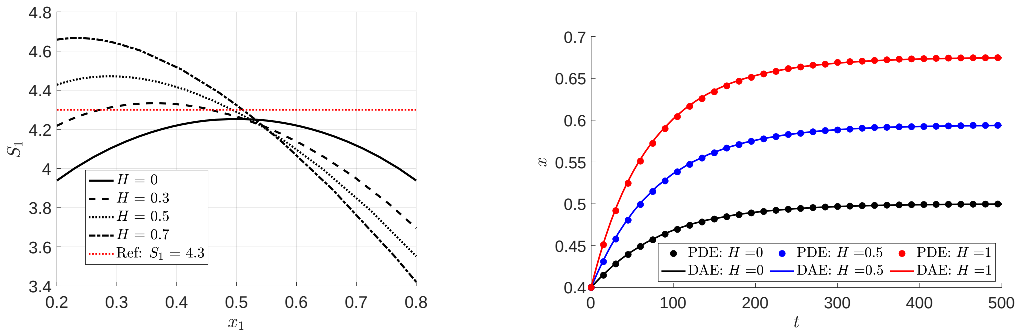

(a) Source strength of a one-spot pattern **(b)** x-coordinate of spot trajectories

Figure 3: Left panel: For $\varepsilon = 0.02$ and $a = 36$ in (4.1a), we plot S_1 versus x_1 for various values of H along the midline of the unit square. Right panel: We fix $\varepsilon = 0.02$, $a = 32$ so that $S_1 < \Sigma_2 \approx 4.3$ and no spot-splitting occurs. The curves from bottom to top are the x-coordinates of the spot trajectory from simulations (full PDE (1.1), solid curves; DAE (4.1), solid markers) for $H = 0$, $H = 0.5$ and $H = 1$, respectively. We do not show the y-coordinates of the spot. Both PDE and DAE simulations show that the y-coordinates are very close to $y = 1/2$.

simulation that S_1 alone may not indicate the final fate of the spot. Let $H = 0.5$, $\varepsilon = 0.02$, and $a = 36$, and consider a one-spot pattern with a spot initially centered at $\mathbf{x}_1 = (0.2, 1/2)^T$. From Fig. 3a we observe that $S_1 > \Sigma_2$. The full PDE simulation of (1.1) for this one-spot configuration is shown in Fig. 4. From this figure, we initially observe the peanut-shaped deformation as predicted by our linear stability theory. However, as the spot slowly drifts to the right along the midline of the square, the deformation gradually disappears as the source strength decreases below Σ_2 (see Fig. 3a). Eventually, the single spot reaches its steady-state location. This example shows that the slow dynamics of the one-spot pattern can lead to a spot drifting outside the parameter range where it is predicted to be linearly unstable to a local shape-deforming instability.

(a) $t = 2$ **(b)** $t = 40$ **(c)** $t = 120$ **(d)** $t = 190$

Figure 4: We fix $\varepsilon = 0.02$, $H = 0.5$ and $a = 36$ for a one-spot pattern. The spot is initially centered at $x_1 = 0.2$ on the midline $y = 1/2$, for which the initial source strength S_1 exceeds the threshold Σ_2. This results in the initial peanut-shaped deformation of the spot at $t = 40$. However, as the spot slowly drifts to the right along the midline, S_1 eventually decreases below Σ_2 (see Fig. 3a), and no spot self-replication event occurs.

Next, we study the one-spot steady-state solution. We denote the equilibrium spot location as $\mathbf{x}_e = (x_e, 1/2)^T$, so that from (4.1b) x_e satisfies the nonlinear equation

$$K\Big(a - S_1/2 - \mu(S_1)\Big) - 2\pi S_1 \partial_x R(\mathbf{x}_e; \mathbf{x}_e) = 0\,, \tag{4.2}$$

subject to the constraint (4.1a) for $\mathbf{x}_1 = \mathbf{x}_e$. The linear stability analysis of §3 predicts that the steady-state one-spot solution will be linearly stable to local peanut-shape deformations only if $S_1 < \Sigma_2 \approx 4.3$.

In Fig. 5a we show that the equilibrium location of the spot changes significantly with H, but not with a. In Fig. 5b, we plot the corresponding source strength S_1 for various values of H. There are two main observations from this figure. For fixed H, S_1 increases with a, while for a fixed value of a, S_1 decreases with H. As a result, we predict that a steady-state spot can be stabilized by an increase in the terrain slope gradient H. In Fig. 5c we plot the linear stability region, where $S_1 < \Sigma_2$, in the a versus H parameter space.

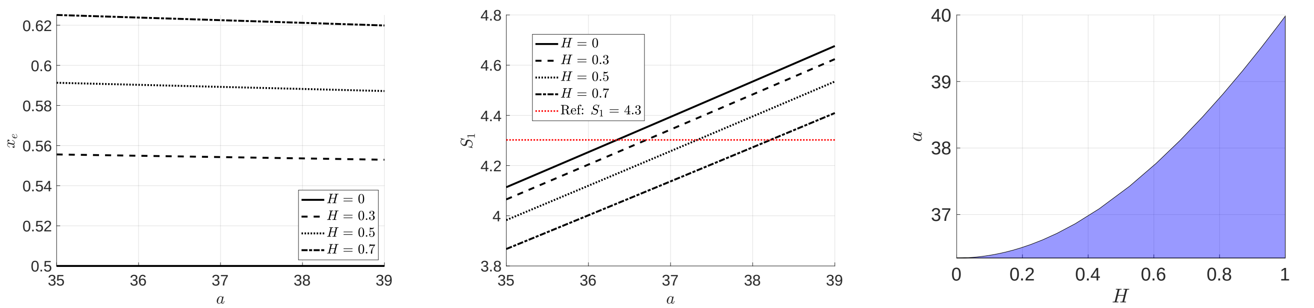

(a) Equilibrium position x_1 **(b)** Source strength S_1 at equilibrium **(c)** Stability region (shaded)

Figure 5: A steady-state one-spot solution with spot location at $\mathbf{x}_e = (x_e, 1/2)^T$ and source strength S_1 when $\varepsilon = 0.02$. Left panel: The x-coordinates of the equilibrium position versus the rainfall rate a for various H. Middle panel: The source strength S_1 at the steady-state location. Right panel: The blue-shaded linear stability region is where $S_1 < \Sigma_2$ in the a versus H parameter space.

The linear stability prediction based on S_1 is more accurate for the steady-state solution as compared to quasi-equilibrium spot patterns, due to the absence of slow dynamics. In Fig. 6, we consider a one-spot steady-state solution with $H = 0.5$ and $a = 39$, for which $S_1 > \Sigma_2$. We predict that the one-spot solution is unstable to a local peanut-shaped deformation. Our prediction is confirmed by the full PDE simulation of (1.1) given in Fig. 6, which shows that the linear instability triggers a nonlinear spot-splitting event.

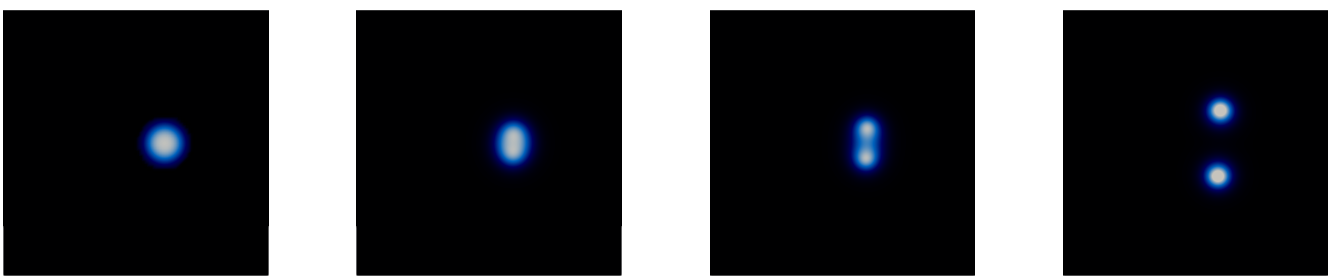

(a) $t = 0$ **(b)** $t = 98$ **(c)** $t = 124$ **(d)** $t = 148$

Figure 6: We fix $\varepsilon = 0.02$, $H = 0.5$ and $a = 39$, for which $S_1 \approx 4.485 > \Sigma_2$. The single spot is initially at its steady-state location $x_{1e} \approx 0.6077$ on the midline $y = 1/2$. The steady-state spot is predicted to be unstable to a local peanut-shape deformation. PDE simulations of (1.1) shows that the linear instability triggers spot-splitting.

Next, we show two full PDE simulations of (1.1) that highlight how the terrain gradient H can lead to different steady-state two-spot patterns after a single spot undergoes a spot-splitting event. We consider a single spot centered at $\mathbf{x}_1 = (0.6, 1/2)^T$ with $a = 40$ and $\varepsilon = 0.02$. In Figs. 7 and 8, we show full PDE simulations of (1.1) with $H = 0.4$ and $H = 0.7$, respectively. Although the single spot splits into two spots for both values of H, we observe that the resulting two-spot quasi-equilibrium pattern tends to very different steady-state configurations as time increases. The theoretical explanation for this behavior long-time behavior is given below in Fig. 9a of §4.2.

4.2 Two-spot patterns

Next, we consider two-spot patterns in the unit square, with spots centered at $\mathbf{x}_1 = (x_1, y_1)^T$ and $\mathbf{x}_2 = (x_2, y_2)^T$. From the NAS (2.26), the two source strengths, S_1 and S_2, satisfy the nonlinear system

$$S_j + 2\pi\nu \left(S_j R(\mathbf{x}_j; \mathbf{x}_j) + S_i e^{K(x_i - x_j)} F(\mathbf{x}_j; \mathbf{x}_i) \right) + \nu\chi(S_i) = \nu a \,, \quad i \neq j \,, \quad i, j = 1, 2 \,. \tag{4.3a}$$

In particular, we are interested in determining the steady-state locations of the two spots, which we label by $\mathbf{x}_{1e} = (x_{1e}, y_{1e})^T$ and $\mathbf{x}_{2e} = (x_{2e}, y_{2e})^T$. From the steady-state of the slow dynamics (2.30), they satisfy

$$K\Big[a - S_j/2 - \mu(S_j)\Big]\mathbf{e}_1 - 2\pi \left[S_j \nabla_{\mathbf{x}} R(\mathbf{x}_{je}; \mathbf{x}_{je}) + S_i e^{K(x_{ie} - x_{je})} \nabla_{\mathbf{x}} F(\mathbf{x}_{je}; \mathbf{x}_{ie}) \right] = \mathbf{0} \,, \quad i \neq j \,, \quad i, j = 1, 2 \,, \tag{4.3b}$$

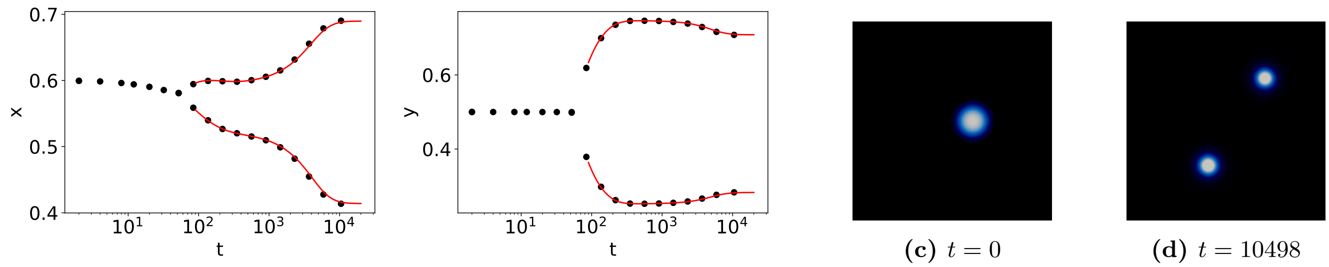

(a) x-coordinate of the spots **(b)** y-coordinate of the spots **(c)** $t = 0$ **(d)** $t = 10498$

Figure 7: $H = 0.4$, $a = 40$, $\varepsilon = 0.02$, with the initial spot location $\mathbf{x}_1 = (0.6, 0.5)^T$. After spot-splitting, there is a very favorable comparison between the trajectories of the two spots from the DAE (2.30) (red solid curve) and from the PDE simulation of (1.1) (black markers).

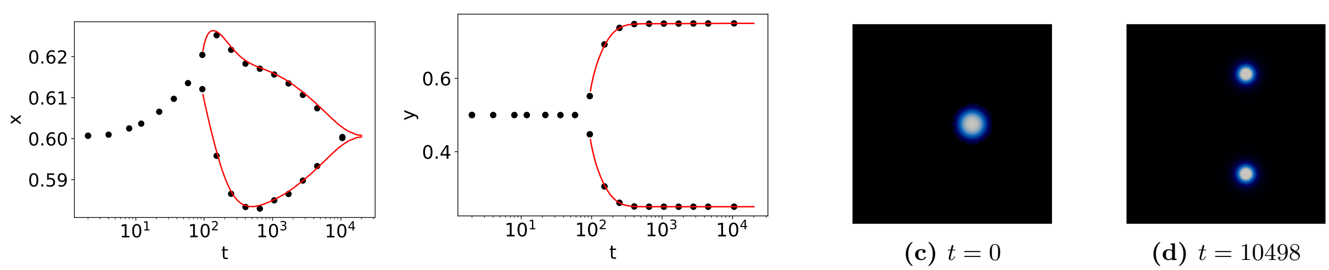

(a) x-coordinate of the spots **(b)** y-coordinate of the spots **(c)** $t = 0$ **(d)** $t = 10498$

Figure 8: Same caption as in Fig. 7 except that H is increased to $H = 0.7$. The two steady-state spots are now vertically aligned.

with $K = H/2$, which is coupled to (4.3a). We remark that, due to the reflective symmetry across the midline $y = 1/2$, another two-spot equilibrium configuration is where $\tilde{\mathbf{x}}_{1e} = (x_{1e}, 1 - y_{1e})^T$ and $\tilde{\mathbf{x}}_{2e} = (x_{2e}, 1 - y_{2e})^T$. We will choose a parameter range of the rainfall rate a for which the two-spot steady-state pattern is linearly stable to local peanut-shaped deformations.

We fix $\varepsilon = 0.02$ and $a = 40$, and study how the terrain gradient H influences the steady-state locations of the two spots. When $H = 0$, the steady-state spots are centered on one of the diagonals of the unit square. In Fig. 9, we plot the difference between the x-coordinates of the two spots versus H. As H increases, the steady-state locations of both spots shift in the uphill direction, while the distance between the two spots in the x-direction decreases with increasing H (see Fig. 9a). At the critical value $H = H_c \approx 0.6076$, the two-spot steady-state pattern becomes vertically aligned in that $x_{1e} = x_{2e}$. For $H > H_c$, the two-spot pattern remains vertically aligned and is given by $x_{1e} = x_{2e}$, $\{y_{1e}, y_{2e}\} = \{1/4, 3/4\}$, with $S_{1e} = S_{2e}$. This observed bifurcation in the steady-state locations for two-spot equilibria as H is varied is the mechanism underlying the full PDE results shown in Fig. 7 and Fig. 8.

The bifurcation behavior in the terrain slope gradient H shown in Fig. 9 can be interpreted qualitatively for the Klausmeier model (1.1). There are two ecological mechanisms that determine a steady-state spot pattern. Firstly, vegetation patches tend to be as far apart as possible so as to minimize the competition for the water resource. For small H, this leads to patches along the diagonals of the square. Secondly, the patches prefer to be located on the uphill portion of the terrain slope in the search of water. This second factor is enhanced by increasing H.

By determining the threshold H_c versus a when $\varepsilon = 0.02$ from (4.3), in Fig. 10 we plot the region in the a versus H parameter space where the vertically aligned two-spot equilibrium is linearly stable as a steady-state of the DAE dynamics (2.30) (see Proposition B.1 of Appendix B for the linear stability formulation). From Fig. 10 we observe that H_c increases with a. Therefore, vertically aligned 2-spot equilibria are stabilized by small a, or large H.

To confirm the predictions of Fig. 10, we present PDE simulation results of (1.1) for $\varepsilon = 0.2$ when the initial locations of the two spots are at $(0.3, 0.3)$ and $(0.7, 0.7)$. The parameter pairs $(a, H_1) = (46, 0.64)$ and $(a, H_2) = (46, 0.62)$ lie inside and outside the stability region, respectively. The PDE simulation results reported in Fig.11 show that when $H_1 = 0.64$ the two-spot quasi-equilibrium pattern tends to a vertically aligned spot configuration. In contrast, when $H_1 = 0.62$, the steady-state two-spot pattern is not vertically aligned, i.e. $x_{1e} \neq x_{2e}$. When

$a = 46$, the predicted threshold for the onset of vertical alignment from Fig. 10 is $H_c \approx 0.631$.

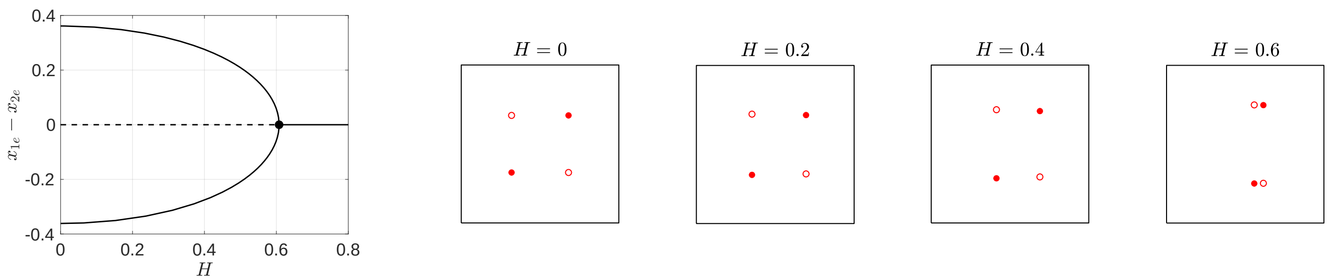

Figure 9: For $\varepsilon = 0.02$ and $a = 40$, the steady-state locations for a two-spot pattern, labeled by $(x_{1e}\,, y_{1e})$ and $(x_{2e}\,, y_{2e})$, in the unit square computed from the steady-state DAE system (4.3) as H is varied. Left panel: The bifurcation diagram of $x_{1e} - x_{2e}$ versus H. The trivial branch, for which $x_{1e} = x_{2e}$ and $y_{1e} = 0.25, y_{2e} = 0.75$, becomes linearly stable as a solution of the DAE dynamics when $H > H_c \approx 0.6076$. The lower (non-trivial) branch is due to the symmetry across the midline $y = 1/2$. Other panels: Visualization of some two-spot equilibria (either open or filled circles) corresponding to the left-panel.

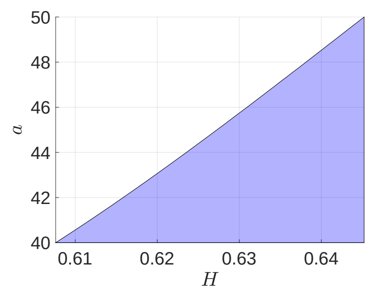

Figure 10: Linear stability (blue) region for a vertically aligned two-spot steady-state in the a versus H parameter space, as computed from (4.3). In the blue shaded region the two-spot equilibrium is linearly stable as a steady-state of the DAE dynamics (2.30). The boundary is the bifurcation threshold $H_c = H_c(a)$ that predicts the minimum value of H where vertical alignment of two-spot steady-states occurs.

4.3 Three-spot patterns

Next, we study three-spot equilibrium configurations of the form $\left\{(x_{1e}\,, 1/2)^T\,, (x_{2e}\,, y_{2e})^T\,, (x_{2e}\,, 1 - y_{2e})^T\right\}$ in the unit square, for which one spot is on the midline $y = 1/2$ while the other two spots are aligned vertically at $x = x_{2e}$. There are three possible such steady-state patterns; either $x_{1e} < x_{2e}$ (more spots on the right), $x_{1e} > x_{2e}$ (more spots on the left), or $x_{1e} = x_{2e}$ (all spots are vertically aligned). We now consider each possibility.

4.3.1 Cases $x_{1e} < x_{2e}$ or $x_{1e} > x_{2e}$

We first fix $\varepsilon = 0.02$ and $a = 60$, and numerically compute x_{1e}, x_{2e} and y_{2e} from the steady-state of the DAE dynamics (2.30) coupled to the NAS (2.26) with H chosen as the continuation variable. The results for the two cases $x_{1e} < x_{2e}$ and $x_{1e} > x_{2e}$ are shown in Fig. 12 on the range $0 < H < 2$. By using the criterion in Proposition B.1 of Appendix B, the three-spot equilibrium configurations in Fig. 12a and Fig. 12b with $x_{1e} < x_{2e}$ are all linearly stable as steady-states of the DAE dynamics (2.30) and (2.26). In contrast, for the case $x_{1e} > x_{2e}$, we observe from Fig. 12c and Fig. 12d that there is a saddle-node bifurcation at $H = H_f \approx 1.7497$. In Fig. 12c and Fig. 12d, steady-state configurations along the solid branch are linearly unstable as equilibria of the DAE dynamics (2.30) and (2.26), as predicted by the criterion in Proposition B.1 of Appendix B. However, along the dashed branches in Fig. 12c and Fig. 12d three-spot equilibria are all unstable due to a positive real eigenvalue for the GCEP (3.15b). This unstable eigenvalue of the GCEP leads to a competition instability in the amplitude of the spots and occurs on an $\mathcal{O}(1)$ time-scale that is fast in comparison with the relatively weak $\mathcal{O}(\varepsilon^{-2})$ time-scale instabilities arising from unstable steady-states of the DAE dynamics (2.30) and (2.26).

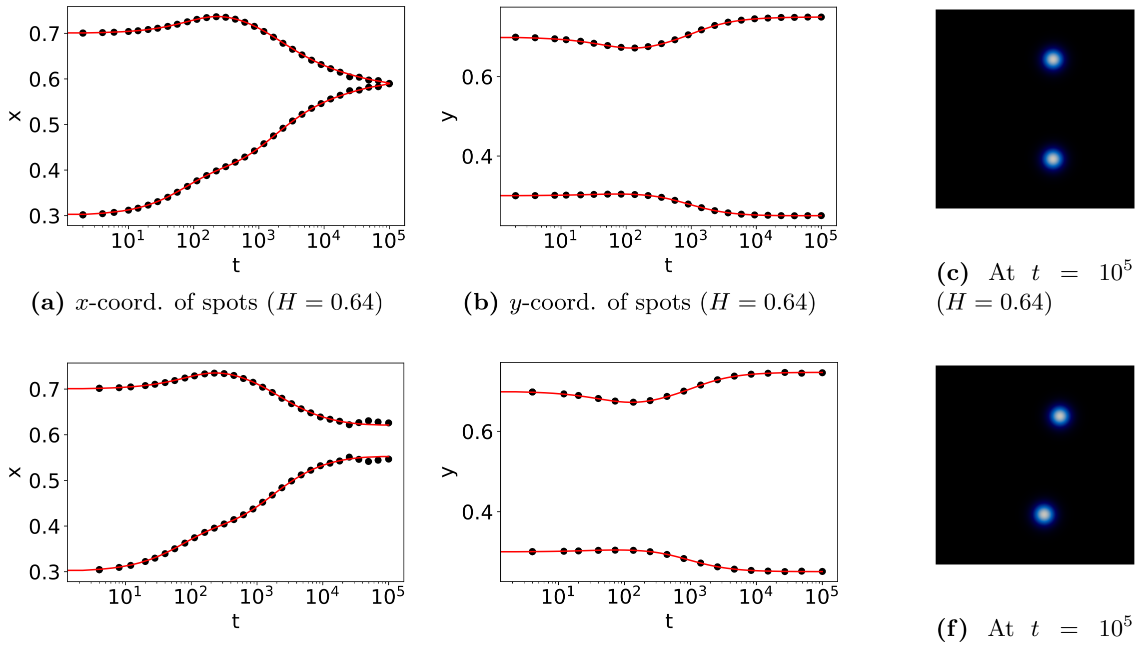

(a) x-coord. of spots ($H = 0.64$) **(b)** y-coord. of spots ($H = 0.64$) **(c)** At $t = 10^5$ ($H = 0.64$)

(d) x-coord. of spots ($H = 0.62$) **(e)** y-coord. of spots ($H = 0.62$) **(f)** At $t = 10^5$ ($H = 0.62$)

Figure 11: Full PDE results of (1.1) in the unit square for $a = 46$ and $\varepsilon = 0.02$ for two-spot patterns with the initial spot locations $(0.3, 0.3)^T$ and $(0.7, 0.7)^T$. For $H = 0.64$, there is a very favorable comparison between the full PDE results (black markers) and the DAE results (solid red curves), as computed from (2.30), for the x and y coordinates of the two-spot pattern as shown in (a) and (b), respectively. A similar comparison for $H = 0.62$ is shown in (d) and (e). At $t = 10^5$, the two-spot quasi-equilibria become very close to their steady-states, as shown in (c) and (f) for $H = 0.64$ and $H = 0.62$, respectively. Vertical alignment occurs only for $H = 0.64$. From Fig. 10, the predicted threshold for vertical alignment from the asymptotic theory is $H_c \approx 0.631$ when $a = 46$.

As a partial confirmation of the results in Fig. 12, we verify from a full PDE simulation of (1.1) that a three-spot equilibrium solution represented by the point on the dashed branch in Figs. 12c–12d is unstable on an $\mathcal{O}(1)$ time-scale due to a competition instability. We set $H = 1$, $\varepsilon = 0.02$, and consider a three-spot initial state where $x_{1e} \approx 0.9046$, $x_{2e} \approx 0.5630$, and $y_{2e} \approx 0.7635$. The snapshots of the PDE simulation of (1.1) in Fig. 13 show that the weaker spot on the uphill side of the terrain slope gradient is rapidly annihilated, which agrees with our prediction based on the GCEP.

Next, we set $H = 0.5$ and $\varepsilon = 0.02$ and perform a full PDE simulation of (1.1) with three spots initially located at $\mathbf{x}_1 = (1/2, 1/2)^T$, $\mathbf{x}_2 = (1/2, 5/6)^T$ and $\mathbf{x}_3 = (1/2, 1/6)^T$. Some snapshots for the v-component are shown in Fig. 14. We observe that, although the three-spot pattern first approaches the unstable equilibrium locations indicated in Figs. 12c and 12d, the pattern slowly rotates and settles to the stable equilibrium configuration indicated in Fig. 12a, 12b where two spots are on the uphill side of the terrain gradient. This computation provides confirmation that the equilibrium configurations indicated by Figs. 12a and 12b (Figs. 12c, 12d) are linearly stable (unstable).

4.3.2 Case $x_{1e} = x_{2e}$

Next, we study the linear stability of equilibrium three-spot configurations that are vertically aligned with spots centered at $\{(x_{1e}, 1/2)^T, (x_{1e}, 5/6)^T, (x_{1e}, 1/6)^T\}$, where the y coordinates are due to the Neumann conditions on the boundary of the unit square. For $\varepsilon = 0.02$, in Fig. 15 we plot x_{1e} versus either the slope gradient H (with $a = 58.231$) or the rainfall rate a (with $H = 0.5077$), as obtained by path-following these equilibria from the steady-states of the DAE dynamics (2.30) and (2.26). We obtain that all of these equilibria in Fig. 15 are linearly unstable. For Fig. 15a, the criterion (B.1) in Proposition B.1 of Appendix B predicts that the steady-states are unstable as equilibria of the DAE dynamics (2.30) and (2.26) on the entire range $0 < H < 2$. Along the dashed part of the solution branch in Fig. 15b, three-spot equilibria are unstable due to a positive root of the GCEP (3.15b), which leads to a competition instability. In contrast, at each point on the solid part of this branch, a three-spot equilibrium is unstable as a steady-state of the slow dynamics (2.30) and (2.26).

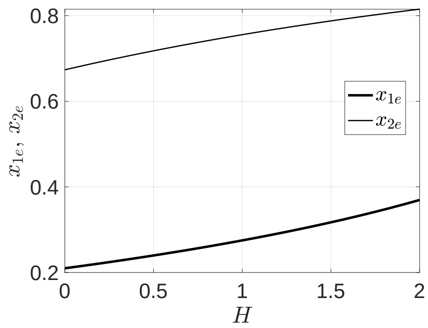

(a) $x_{1e}\,, x_{2e}$ versus H $(x_{1e} < x_{2e})$

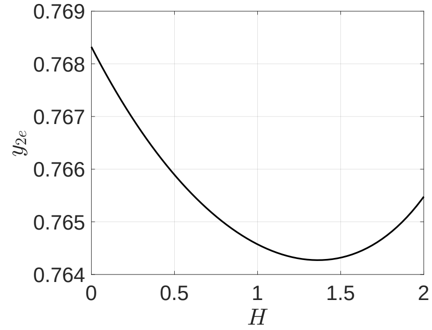

(b) y_{2e} versus H $(x_{1e} < x_{2e})$

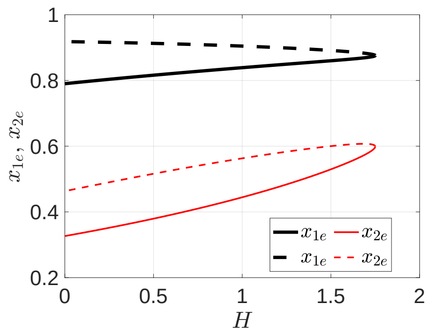

(c) $x_{1e}\,, x_{2e}$ versus H $(x_{1e} > x_{2e})$

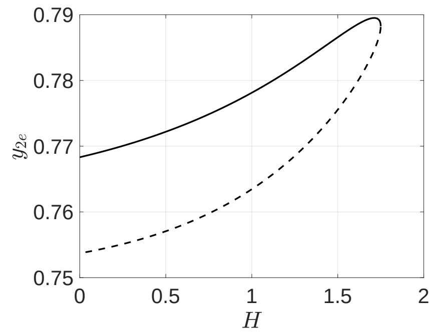

(d) y_{2e} versus H $(x_{1e} > x_{2e})$

Figure 12: For $\varepsilon = 0.02$ and $a = 60$, steady-state three-spot patterns of the form $\left\{(x_{1e}\,, 1/2)^T\,, (x_{2e}\,, y_{2e})^T\,, (x_{2e}\,, 1-y_{2e})^T\right\}$ in the unit square are computed from the steady-state of the DAE dynamics (2.30) and (2.26) as H is varied. In the top and bottom panels, we show the dependence of x_{1e}, x_{2e} and y_{2e} with respect to H for the cases $x_{1e} < x_{2e}$ and $x_{1e} > x_{2e}$, respectively. Branches of equilibria for $x_{1e} < x_{2e}$ (top panels) are all linearly stable. For $x_{1e} > x_{2e}$ (bottom panels), the solid branches are unstable as steady-states of the DAE dynamics. The dashed branches are unstable to spot amplitude perturbations from the GCEP (3.15b).

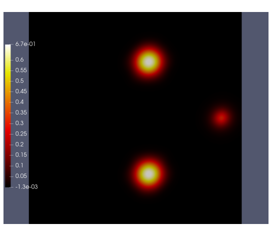

(a) $t = 0.5$

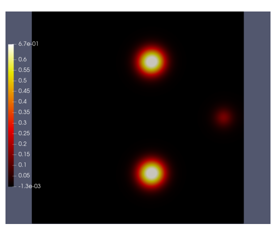

(b) $t = 3$

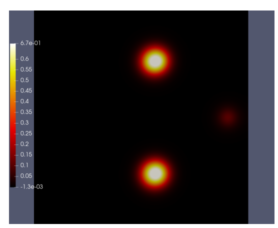

(c) $t = 3.5$

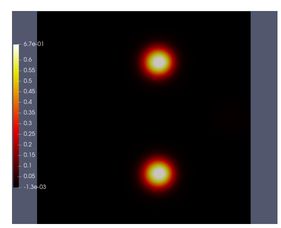

(d) $t = 6$

Figure 13: Full PDE simulation of (1.1) for $H = 1$, $a = 60$, and $\varepsilon = 0.02$ for a three-spot steady-state pattern with spots centered at $(x_{1e}, 1/2)$, (x_{2e}, y_{2e}), and $(x_{2e}, 1-y_{2e})$, with $x_{1e} \approx 0.9046$, $x_{2e} \approx 0.5630$, and $y_{2e} \approx 0.7635$, corresponding to a point on the dashed curves in Figs. 12c and 12d where the steady-state is unstable due to a positive real eigenvalue of the GCEP (3.15b). The snapshots of the v-component in (1.1) show that the weaker spot on the uphill side of the terrain gradient is rapidly annihilated.

We now verify from a full PDE simulation of (1.1) that a three-spot equilibrium on the dashed branch in Fig. 15b with $a = 34.8720$, for which $x_{1e} \approx 0.5687$, is unstable due to a spot amplitude instability. This is confirmed from the snapshots of the PDE simulation shown in Fig. 16. This linear instability is seen to trigger the annihilation of two spots, with only the spot on the midline of the unit square persisting. Although our results have shown that vertically aligned three-spot equilibria are all unstable in the unit square for this range of a and H, we conjecture that with an increase in the domain width it should be possible to stabilize three or more vertically aligned spots.

(a) $t = 0$ **(b)** $t = 200$ **(c)** $t = 400$ **(d)** $t = 1000$

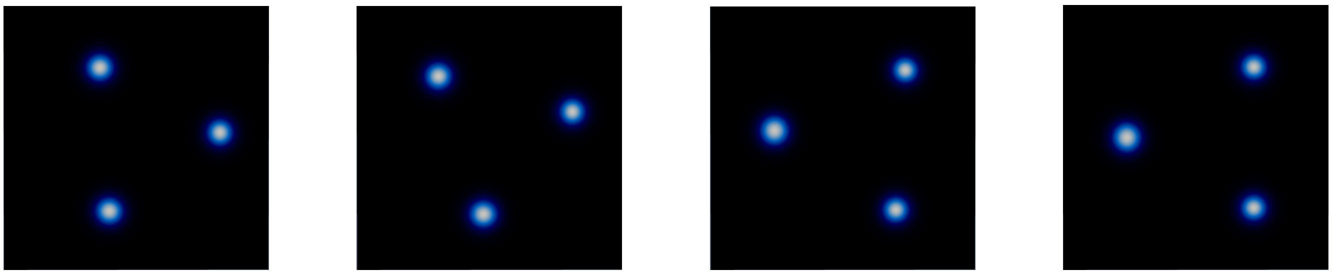

(e) $t = 3000$ **(f)** $t = 4000$ **(g)** $t = 6000$ **(h)** $t = 9980$

Figure 14: Snapshots of full PDE simulations of (1.1) with $H = 1$ and $\varepsilon = 0.02$ for an initial three-spot pattern that is vertically aligned with spots centered at $\mathbf{x}_1 = (1/2, 1/2)^T$, $\mathbf{x}_2 = (1/2, 5/6)^T$ and $\mathbf{x}_3 = (1/2, 1/6)^T$. The vertical alignment breaks down as time increase, with the pattern eventually tending to the linearly stable steady-state in Figs. 12a and 12b after first approaching the unstable steady-state in Figs. 12c and 12d.

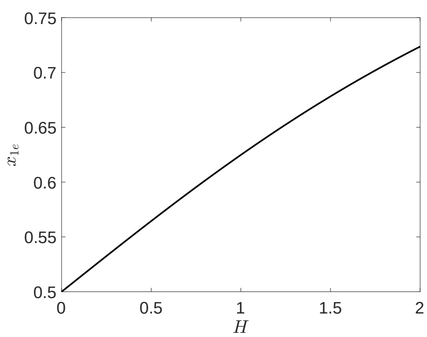

(a) x_{1e} versus H

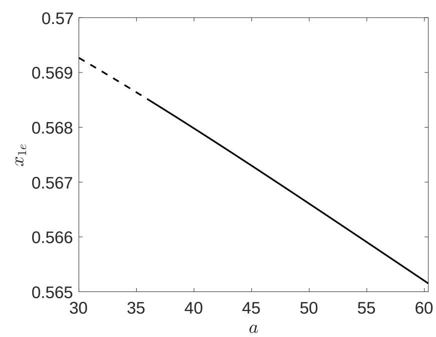

(b) x_{1e} versus a

Figure 15: Steady-states of the DAE dynamics (2.30) and (2.26) for a three-spot equilibrium of the form $\left\{(x_{1e}, 1/2)^T, (x_{1e}, 5/6)^T, (x_{1e}, 1/6)^T\right\}$. Left panel: x_{1e} versus H for $a = 58.231$. These steady-states are unstable as equilibria of the DAE dynamics (2.30) and (2.26). Right panel: x_{1e} versus a with $H = 0.5077$. Along the solid portion the equilibria are unstable for the DAE dynamics, while along the dashed portion ($30 < a < 35.9284$) the spot amplitudes are unstable owing to a positive real eigenvalue of the GCEP (3.15b).

5 Delayed bifurcations due to a time-dependent rainfall rate

In this section we study the slow dynamics and instabilities of multi-spot patterns in the unit square in the presence of a slowly receding rainfall rate. In §3 it was shown that an insufficient rainfall rate can lead to a competition instability, which can trigger a nonlinear spot-annihilation event.

5.1 DAE simulations of spot dynamics with the zero-eigenvalue crossing criterion

We consider the slowly decreasing rainfall rate given by,

$$a = \max\left(a_0 - \delta t,\, a_1\right)\,, \quad \text{with} \quad \delta \ll 1\,, \tag{5.1}$$

(a) $t = 10$ **(b)** $t = 100$ **(c)** $t = 140$ **(d)** $t = 150$

Figure 16: Full PDE simulation of (1.1) with $a = 34.8720$ and $H = 0.5077$ for an initial three-spot steady-state with spots centered at $\{(x_{1e}, 1/2)^T, (x_{1e}, 5/6)^T, (x_{1e}, 1/6)^T\}$, with $x_{1e} = 0.5697$, corresponding to a point on the dashed branch Fig. 15b where a competition instability in the spot amplitudes is predicted. The snapshots of v confirm this linear instability, and that it triggers the annihilation of two spots on an $\mathcal{O}(1)$ time-scale.

where $a_1 > 0$ is the baseline rate. The DAE system for slow spot dynamics is obtained by substituting (5.1) into (2.30) and (2.26). As a decreases, a competition instability of a multi-spot pattern can occur owing to an unstable eigenvalue λ of the GCEP (3.15b) in $\mathrm{Re}(\lambda) > 0$. To detect such an instability, we augment the zero-eigenvalue crossing criterion (3.19) to the DAE dynamics (2.30) and (2.26). If a zero-eigenvalue crossing is detected, we simply remove from the DAE simulation the spot with the smallest source strength.

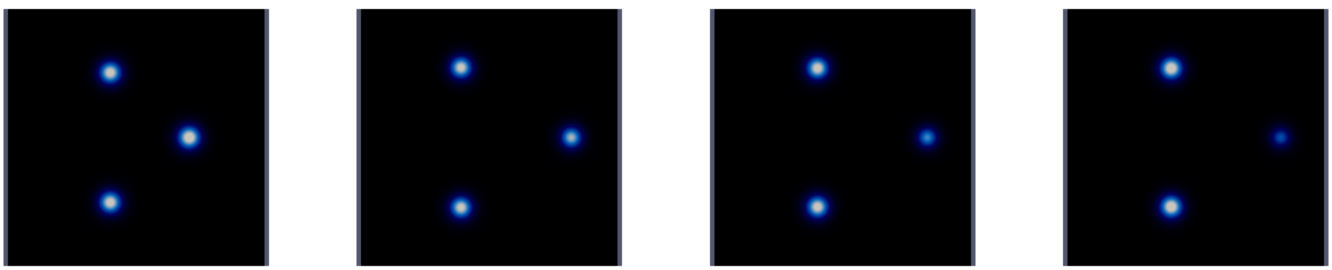

(a) $t = 5$ **(b)** $t = 400$ **(c)** $t = 540$ **(d)** $t = 550$

(e) $t = 555$ **(f)** $t = 600$ **(g)** $t = 800$ **(h)** $t = 1990$

Figure 17: Snapshots of full PDE results for (1.1) with $\varepsilon = 0.02$ and $H = 0.5$. The dynamic rainfall rate is $a = \max(40 - \delta t, 26)$ with $\delta = 0.01$. The initial condition is a spot on the right and two vertically aligned spots on the left. The spot on the midline disappears around $t = 550$, after which the remaining two vertically aligned spots drift slowly up the terrain slope to their steady-state locations.

For our first numerical experiment we let $\varepsilon = 0.02$ and $H = 0.5$, and use (5.1) with $a_0 = 40$, $a_1 = 26$ and $\delta = 0.01$. We consider an initial three-spot pattern with one spot on the midline at $\mathbf{x}_1 = (0.7, 1/2)^T$, and two vertically aligned spots centered at $(0.4, 1/4)^T$ and $(0.4, 3/4)^T$. The DAE simulation of the spot trajectories from (2.30) and (2.26), as shown in Fig. 18, are seen to agree closely with corresponding full numerical results computed from the PDE (1.1). Snapshots in time of the PDE results are shown in Fig. 17. The spot on the midline is found to have a smaller source strength than for the two vertically aligned spots. In the DAE simulation, a zero-eigenvalue crossing for the GCEP (3.19) is first detected at $t \approx 528.33$. At this time the weak spot on the midline is removed, and the DAE simulation is continued in time for the two remaining spots. From (5.1), the rainfall stops decreasing at $t = 1400$, so that $a \equiv 26$ for $t \geq 1400$. In the DAE simulation, we observe from Fig. 18 that the two surviving spots

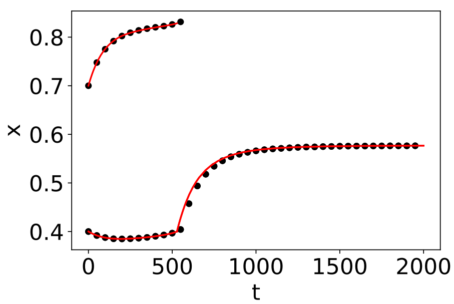

(a) x-coordinates

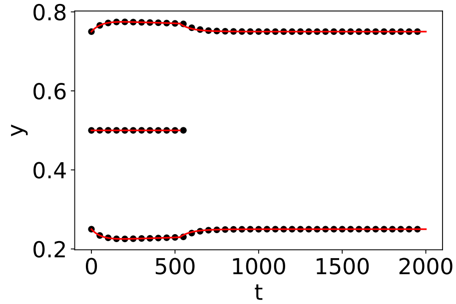

(b) y-coordinates

Figure 18: Comparison of spot trajectories between the DAE simulations of (2.30) and (2.26) (solid lines), with the zero-eigenvalue detection criterion of the GCEP, and the full PDE results from (1.1) (red markers). Parameters as in Fig. 17.

remain vertically aligned and slowly drift up the terrain slope, approaching their steady-state locations at around $t = 1500$. In the full PDE simulation of (1.1), we observe from Fig. 17 that the spot on the midline disappears at $t \approx 550$, which exceeds our predicted time $t \approx 528.33$ for the onset of a competition instability from the GCEP. Although the zero-eigenvalue crossing criterion in the DAE simulation correctly forecasts the annihilation of a spot, we are unable to define the exact time when a spot completely disappears. In the full PDE simulation, it takes an $\mathcal{O}(1)$ time for the competition instability to trigger the nonlinear event that annihilates the weakest spot. The $\mathcal{O}(1)$ time discrepancy between the zero-eigenvalue detection of the GCEP and the actual disappearance of the weakest spot in the PDE simulation is small relative to the long $\mathcal{O}(\varepsilon^{-2})$ time-scale of slow spot dynamics. From Fig. 18 this discrepancy does not sabotage the agreement between the DAE and full PDE results for the trajectories of the spots that persist after the annihilation event.

(a) $t = 5$

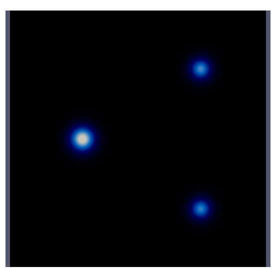

(b) $t = 560$

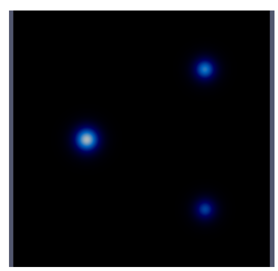

(c) $t = 585$

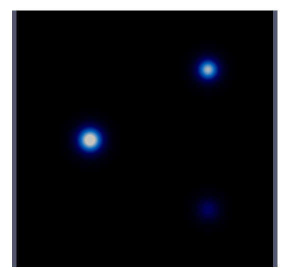

(d) $t = 590$

(e) $t = 1400$

(f) $t = 1445$

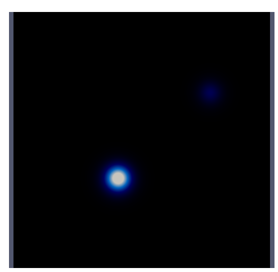

(g) $t = 1450$

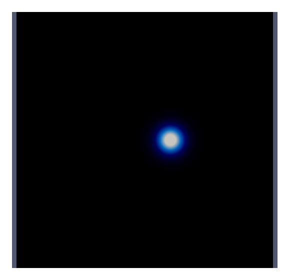

(h) $t = 2490$

Figure 19: Snapshots of full PDE results for (1.1) with $\varepsilon = 0.02$, $H = 0.5$, and dynamic rainfall rate $a = \max(40 - \delta t, 26)$ with $\delta = 0.01$. The initial condition has one spot on the left and two vertically aligned spots on the right. One spot remains on the midline $y = 1/2$ until one of the two vertically aligned spots disappears at around $t = 590$. The two surviving spots undergo another spot-annihilation event at around $t = 1445$. The sole remaining spot then approaches the midline where it slowly drifts up the terrain slope to its steady-state location.

For our second experiment, we again choose $\varepsilon = 0.02$, $H = 0.5$, and the same dynamic rainfall rate ($a_0 = 40$, $\delta = 0.01$, $a_1 = 26$), but with a different initial three-spot pattern with one spot on the midline at $\mathbf{x}_1 = (0.4, 1/2)^T$ and two vertically aligned spots centered at $\mathbf{x}_2 = (0.7, 1/4)^T$ and $\mathbf{x}_3 = (0.7, 3/4)^T$. In the DAE simulation for this

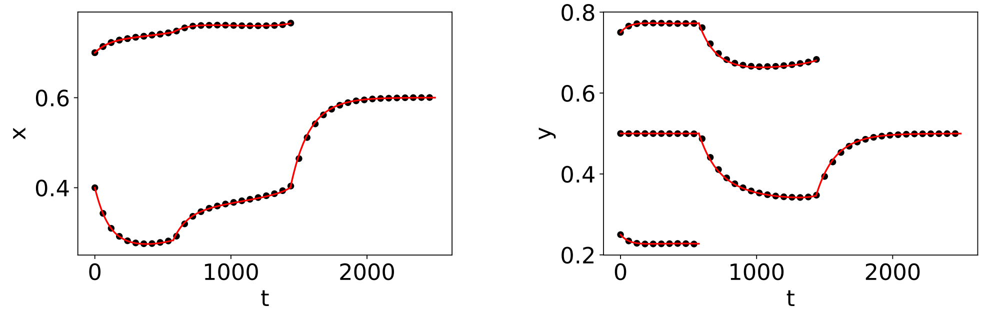

(a) x-coordinates **(b)** y-coordinates

Figure 20: Comparison of spot trajectories between the DAE simulations of (2.30) and (2.26) (solid lines), with the zero-eigenvalue detection criterion of the GCEP, and the full PDE results from (1.1) (red markers). Parameters as in Fig. 19. We observe very good agreement both before and after the two spot-annihilation events.

pattern, a zero-eigenvalue crossing of the GCEP (3.19) is first detected at $t \approx 575.77$, at which time the vertically aligned spots have a common source strength $S_2 = S_3 \approx 1.1526$ that is less than the source strength $S_1 \approx 2.0631$ for the spot on the midline. Although we predict that one of the two vertically aligned spots will be annihilated by the competition instability, due to symmetry we cannot predict which one disappear. In the full PDE simulations of (1.1) it is small discretization errors that determine the specific fate of the two vertically aligned spots. From the snapshots of the PDE simulation shown in Fig. 19 we observe that it is the bottom one of the vertically aligned spots that is annihilated around $t = 585$. In our DAE algorithm, we remove this same spot at $t = 575.77$ and continue the DAE simulation in time for the remaining two spots until we detect a second zero-eigenvalue crossing of the GCEP at $t \approx 1437.34$. Upon removing the weaker spot (the upper right spot in Fig. 19e), the DAE simulation shows that the sole remaining spot slowly drifts up the terrain slope to its steady-state location on the midline. The very favorable comparison shown in Fig. 20 between the spot trajectories computed from the DAE and the full PDE (1.1) confirm that our DAE simulations, augmented by the the spot removal algorithm based on the GCEP criterion (3.19), can accurately predict slow spot dynamics both before and after spot-annihilation events.

For our final experiment, we choose $\varepsilon = 0.02$, $H = 1$, and a dynamic rainfall rate (5.1) with $a_0 = 70$, $a_1 = 55$, and $\delta = 0.01$. We consider an initial five-spot pattern with a spot on the midline $\mathbf{x}_1 = (0.2, 1/2)^T$, one pair of vertically aligned spots at $\mathbf{x}_2 = (0.5, 1/4)^T$ and $\mathbf{x}_3 = (0.5, 3/4)^T$, and another such pair centered at $\mathbf{x}_4 = (0.8, 1/4)^T$ and $\mathbf{x}_5 = (0.8, 3/4)^T$. Among these five spots, the rightmost vertically aligned pair of spots have the smallest source strengths. In our DAE simulation the first zero-eigenvalue crossing of the GCEP (3.19) is detected at $t \approx 1011.36$, from which we predict that one of the two rightmost spots will be annihilated. As shown in the snapshots in Fig. 21 of the full PDE simulation of (1.1), it is the top of the rightmost pair of spots that disappears around $t = 1010$. As such, we remove this spot and continue the DAE simulation for the remaining four spots until a second zero-eigenvalue crossing for the GCEP is detected at $t \approx 1285.89$. From Fig. 21f, it the lower-right spot that disappears around $t = 1285$. Once again, we remove the corresponding spot and continue the DAE simulation for the remaining three spots until they reach their steady-state locations. The rainfall rate becomes fixed at $a \equiv 55$ for $t \geq 1500$. The favorable comparison shown in Fig. 22 between the DAE and full PDE results for the spot trajectories illustrates that our DAE algorithm accurately detects the onset of spot-annihilation events during the slow dynamics of multi-spot quasi-equilibria.

5.2 Asymptotic analysis of delayed spot annihilation

In some of our PDE simulation results in §5.1 it was observed that there is a time delay for the annihilation of a spot after the detection of a zero-eigenvalue crossing for the GCEP (3.15b). In this subsection, we analyze this delay behavior for a single steady-state spot centered at the midpoint $\mathbf{x}_1 = (1/2, 1/2)^T$ of the unit square for the special case of no slope gradient $H = 0$ and with $m = 1$. In contrast to the situation with $H > 0$, when there is no slope gradient the location of the steady-state spot remains at $\mathbf{x}_1$ as the rainfall rate a is ramped slowly in time.

The Klausmeier RD system (1.1) with $H = 0$ and $m = 1$ is

$$v_t = \varepsilon^2 \Delta v - v + uv^2 \,, \quad u_t = \Delta u - u + a - \varepsilon^{-2} uv^2 \,, \quad \text{in } \Omega \,; \qquad \partial_n v = \partial_n u = 0 \,, \quad \text{on } \partial\Omega \,. \tag{5.2}$$

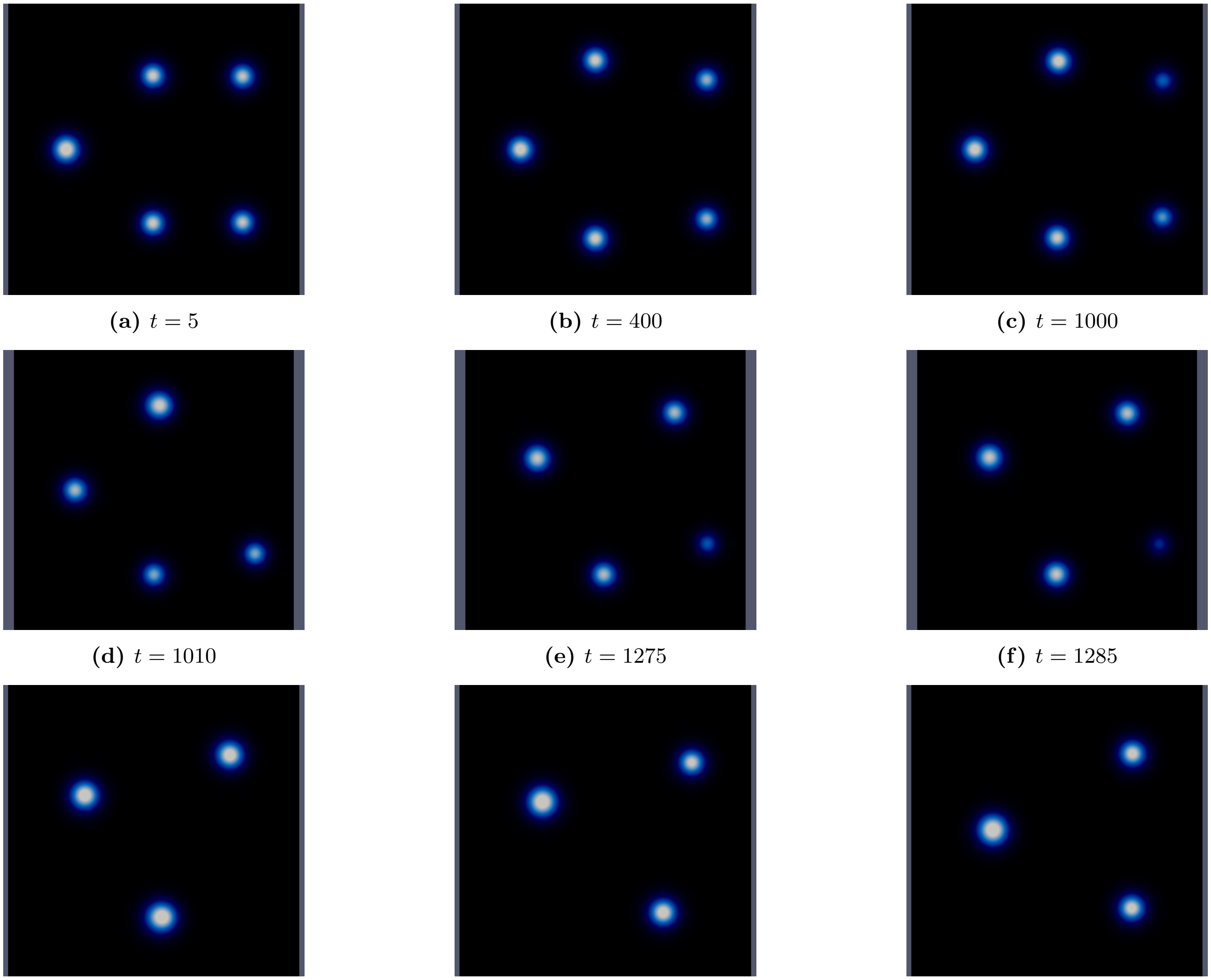

(a) $t = 5$ **(b)** $t = 400$ **(c)** $t = 1000$

(d) $t = 1010$ **(e)** $t = 1275$ **(f)** $t = 1285$

(g) $t = 1300$ **(h)** $t = 1585$ **(i)** $t = 3390$

Figure 21: Snapshots of full PDE results for (1.1) with $\varepsilon = 0.02$, $H = 1.0$, and the dynamic rainfall rate $a = \max(70 - \delta t, 55)$ with $\delta = 0.01$. The five-spot initial pattern has one spot on the left and two pairs of vertically aligned spots. Two spot-annihilation events occur at later times and the final steady-state has a spot on the midline and a pair of vertically aligned spots on the uphill side of the terrain slope.

In Fig. 23 we show the saddle-node bifurcation structure for the existence of the one-spot steady-state solution of (5.2) as a is varied. From the scalar NAS (4.1a), the asymptotic theory predicts that the saddle-node point occurs at the critical value $a = a_c \approx 13.205$ when $\varepsilon = 0.02$, with no one-spot steady-state existing on the range $a < a_c$. In our analysis below, we will consider a slowly varying rainfall rate with

$$a = a_c - \varepsilon t \,, \tag{5.3}$$

and we will derive a normal form ODE to characterize a delayed transition for the annihilation of the quasi steady-state spot as time increases.

To this end, we introduce a slow time scale $\tau = \varepsilon^{-q} t$, with $q < 0$ to be determined, together with the expansion

$$v = v_c + \varepsilon^p v_1 + \varepsilon^{2p} v_2 + \cdots \,, \qquad u = u_c + \varepsilon^p u_1 + \varepsilon^{2p} u_2 + \cdots \,, \tag{5.4}$$

where v_c and u_c denote the steady-state solution when $a = a_c$, which satisfies

$$\varepsilon^2 \Delta v_c - v_c + u_c v_c^2 = 0 \,, \qquad \Delta u_c - u_c + a_c - \varepsilon^{-2} u_c v_c^2 = 0 \,, \quad \text{in } \Omega \,, \qquad \partial_n u = \partial_n v = 0 \,, \quad \text{on } \partial\Omega \,. \tag{5.5}$$

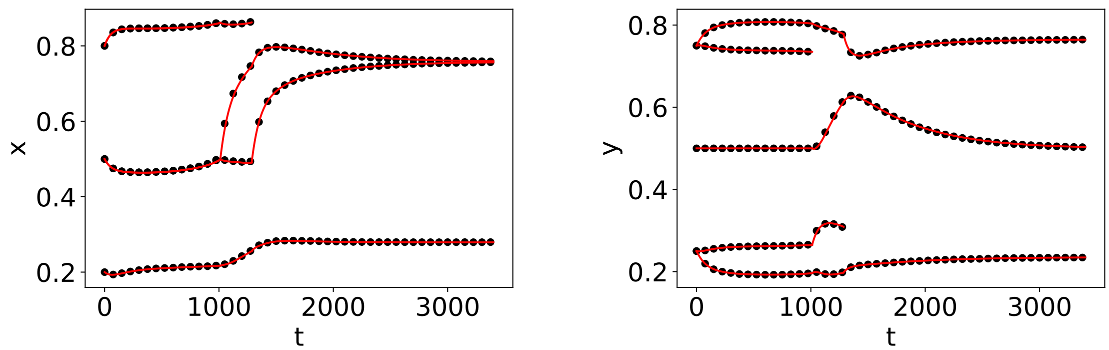

Figure 22: Same caption as in Fig. 20 except that the parameters now correspond to the initial five-spot pattern shown in Fig. 21. The spot trajectories from the DAE simulations and the PDE (1.1) compare very favorably both before and after the two spot-annihilation events.

The exponents p and q will be determined below from an asymptotic balance.

By substituting (5.4) into the v-equation in (5.2) we obtain

$$\begin{aligned} \varepsilon^{p-q}\partial_\tau v_1 + \cdots = \varepsilon^2 \Delta v_c - v_c + u_c\, v_c^2 + \varepsilon^p \left(\varepsilon^2 \Delta v_1 - v_1 + 2\, u_c\, v_c\, v_1 + v_c^2\, u_1\right) \\ + \varepsilon^{2p} \left(\varepsilon^2 \Delta v_2 - v_2 + 2\, u_c\, v_c\, v_2 + v_c^2\, u_2 + 2\, v_c\, u_1\, v_1 + u_c\, v_1^2\right) . \end{aligned} \tag{5.6}$$

To balance the slow time derivative of v_1 with the problem for v_2 we take

$$p - q = 2p \qquad \text{so that} \qquad p = -q\,. \tag{5.7}$$

Next, we substitute (5.4) into the u-equation in (5.2) to get

$$\begin{aligned} \varepsilon^{p-q}\partial_\tau u_1 = \Delta u_c - u_c + a_c - \varepsilon^{1+q}\tau - \varepsilon^{-2} u_c\, v_c^2 + \varepsilon^p \left[\Delta u_1 - u_1 - \varepsilon^{-2}\left(2\, u_c\, v_c\, v_1 + v_c^2\, u_1\right)\right] \\ + \varepsilon^{2p}\left[\Delta u_2 - u_2 - \varepsilon^{-2}\left(2\, u_c\, v_c\, v_2 + v_c^2\, u_2 + 2\, v_c\, u_1\, v_1 + u_c\, v_1^2\right)\right] . \end{aligned} \tag{5.8}$$

To balance the linear ramp in a with the problem for u_2 we further choose that

$$1 + q = 2p\,,$$

so that, together with (5.7), we conclude that

$$p = 1/3\,, \quad \text{and} \quad q = -1/3\,. \tag{5.9}$$

From (5.6) and (5.8), we get that the leading order problem is (5.5). By introducing the local variable $\mathbf{y} = \varepsilon^{-1}\left(\mathbf{x} - \mathbf{x}_1\right)$ and $\rho = |\mathbf{y}|$, the inner problem for (5.5) is simply the core problem (see (2.4)), defined on $\rho > 0$ by

$$\Delta_\rho V_0 - V_0 + U_0 V_0^2 = 0\,, \quad \Delta_\rho U_0 - U_0 V_0^2 = 0\,; \qquad V_0 \to 0\,, \quad U_0 \sim S \log\rho + \chi(S)\,, \quad \text{as} \quad \rho \to \infty\,, \tag{5.10}$$

where $\Delta_\rho \equiv \partial_{\rho\rho} + \rho^{-1}\partial_\rho$, which is to be evaluated at $S = S_c$ corresponding to the saddle-node point $a = a_c$. At $S = S_c$, the solution to (5.10) is denoted by $V_0 = V_c$ and $U_0 = U_c$, and we identify $S_c = \int_0^\infty U_c V_c^2 \rho\, d\rho$.

At next order, the $\mathcal{O}(\varepsilon^p)$ problem for v_1 and u_1 is

$$\varepsilon^2 \Delta v_1 - v_1 + 2u_c v_c v_1 + v_c^2 u_1 = 0\,, \qquad \Delta u_1 - u_1 - \varepsilon^{-2}\left(2u_c v_c v_1 + v_c^2 u_1\right) = 0\,, \quad \text{in } \Omega\,. \tag{5.11}$$

In the inner region, we let $\rho = \varepsilon^{-1}|\mathbf{x} - \mathbf{x}_1|$, $v_1 \sim V_1(\rho)$ and $u_1 \sim U_1(\rho)$ so that, upon neglecting $\mathcal{O}(\varepsilon^2)$ terms, we obtain when $S = S_c$ that $\mathbf{V}_1 \equiv (V_1, U_1)^T$ satisfies

$$\mathcal{L}\mathbf{V}_1 \equiv \Delta_\rho \mathbf{V}_1 + \mathcal{M}_c \mathbf{V}_1 = \mathbf{0}\,, \quad \text{on} \quad \rho \geq 0\,, \qquad \text{where} \qquad \mathcal{M}_c \equiv \begin{pmatrix} -1 + 2U_c V_c & V_c^2 \\ -2U_c V_c & -V_c^2 \end{pmatrix} . \tag{5.12}$$

Upon differentiating the core problem (5.10) with respect to S, and evaluating it at $S = S_c$, we identify that V_1 and U_1 is the zero-crossing eigenfunction of angular mode $k = 0$ (see the discussion following (3.18) in §3), so that

$$V_1 = A\, \partial_S V_c\,, \quad U_1 = A\, \partial_S U_c\,, \quad \text{when} \quad S = S_c\,, \tag{5.13}$$

where the slow amplitude $A = A(\tau)$ is to be determined. Here, we have labeled $\partial_S V_c \equiv \partial_S V_0|_{S=S_c}$ and $\partial_S U_c \equiv \partial_S U_0|_{S=S_c}$. The homogeneous adjoint problem associated with (5.12) for $\mathbf{V}_1^\star \equiv (V_1^\star, U_1^\star)^T$ is

$$\mathcal{L}^\star \mathbf{V}_1^\star \equiv \Delta_\rho \mathbf{V}_1^\star + \mathcal{M}_c^T \mathbf{V}_1^\star = \mathbf{0}\,, \quad \text{on} \quad \rho \geq 0\,; \qquad V_1^\star \to 0\,, \quad U_1^\star \sim \log\rho + \mathcal{O}(1)\,, \quad \text{as } \rho \to \infty\,. \tag{5.14}$$

The far-field behavior for $U_1^\star$ effectively enforces a normalization condition for the non-trivial solution of (5.14).

To determine the outer problem for u_1 when $S = S_c$, we calculate for $\varepsilon \to 0$ in the sense of distributions that

$$\varepsilon^{-2}\left(2u_c v_c v_1 + v_c^2 u_1\right) \to 2\pi A \frac{d}{dS}\left(\int_0^\infty U_c V_c^2 \rho\, d\rho\right)\delta(\mathbf{x}-\mathbf{x}_1) = 2\pi A \delta(\mathbf{x}-\mathbf{x}_1)\,.$$

In this way, the outer problem for u_1 in (5.11) is

$$\Delta u_1 - u_1 = 2\pi A\delta(\mathbf{x})\,, \quad \text{in } \Omega\,; \qquad \partial_n u_1 = 0\,, \quad \text{on } \partial\Omega\,,$$

which has the solution

$$u_1 = -2\pi A G(\mathbf{x};\mathbf{x}_1)\,. \tag{5.15}$$

Here $A = A(\tau)$ and $G(\mathbf{x};\mathbf{x}_1)$ is the Green's function of (2.18) in the unit square where we set $H = 0$ in (2.18).

At next order, the $\mathcal{O}(\varepsilon^{2p})$ problem from (5.6) and (5.8) is

$$\varepsilon^2 \Delta v_2 - v_2 + 2\, u_c\, v_c\, v_2 + v_c^2\, u_2 + 2\, v_c\, u_1\, v_1 + u_c\, v_1^2 = \partial_\tau v_1\,, \tag{5.16a}$$
$$\Delta u_2 - u_2 - \varepsilon^{-2}\left(2\, u_c\, v_c\, v_2 + v_c^2\, u_2 + 2\, v_c\, u_1\, v_1 + u_c\, v_1^2\right) = \tau + \partial_\tau u_1\,. \tag{5.16b}$$

In the inner region, we let $\rho = \varepsilon^{-1}|\mathbf{x}-\mathbf{x}_1|$, $v_2 \sim V_2(\rho)$ and $u_2 \sim U_2(\rho)$, to derive from (5.16), with an $\mathcal{O}(\varepsilon^2)$ error, that $\mathbf{V}_2 \equiv (V_2, U_2)^T$ satisfies

$$\mathcal{L}\mathbf{V}_2 \equiv \Delta_\rho \mathbf{V}_2 + \mathcal{M}_c \mathbf{V}_2 = \begin{pmatrix} \dot{A}\partial_S V_c - A^2 g(\rho) \\ A^2 g(\rho) \end{pmatrix} \qquad \text{on} \quad \rho \geq 0\,, \tag{5.17a}$$

where we have defined $\dot{A} \equiv dA/d\tau$ and $g(\rho)$ by

$$g(\rho) \equiv A^{-2}\left(2\, V_c\, U_1\, V_1 + U_c\, V_1^2\right) = 2V_c\left(\partial_S U_c\right)\left(\partial_S V_c\right) + U_c\left(\partial_S V_c\right)^2\,. \tag{5.17b}$$

By using the same dominant balance argument used in Appendix A of [26] for the derivation of an amplitude equation characterizing the onset of spot-splitting behavior, we can impose for (5.17a) the far-field behavior

$$V_2 \to 0\,, \qquad U_2' \to 0 \quad \text{as} \quad \rho \to \infty\,. \tag{5.17c}$$

To derive an amplitude equation for A, we invoke a solvability condition on (5.17) by using the adjoint problem (5.14). Upon integrating by parts and using the far-field conditions in (5.14) and (5.17c), we obtain

$$\int_0^\infty \left[(\mathbf{V}_1^\star)^T \mathcal{L}\mathbf{V}_2 - (\mathbf{V}_2)^T \mathcal{L}^\star \mathbf{V}_1^\star\right]\rho\, d\rho = \lim_{\rho\to\infty} \rho\left[V_1^\star V_2' + U_1^\star U_2' - V_2 (V_1^\star)' - U_2 (U_1^\star)'\right]\,,$$

which reduces to

$$\int_0^\infty \left[V_1^\star\left(\dot{A}\partial_S V_c - A^2 g(\rho)\right) + U_1^\star A^2 g(\rho)\right]\rho\, d\rho = -\lim_{\rho\to\infty} U_2\,.$$

This yields the following amplitude equation valid at $S = S_c$:

$$\dot{A}\int_0^\infty (\partial_S V_c) V_1^\star\, \rho\, d\rho - A^2 \int_0^\infty \left(V_1^\star - U_1^\star\right) g(\rho)\, \rho\, d\rho = -U_{2\infty}\,, \qquad \text{where} \qquad U_{2\infty} \equiv \lim_{\rho\to\infty} U_2\,. \tag{5.18}$$

The final step in the analysis is to determine the limiting behavior $U_{2\infty}$ in (5.18) by matching the far-field behavior of the inner solution U_2 with the near-field behavior as $\mathbf{x} \to \mathbf{x}_1$ of the outer approximation for u_2. To derive this outer problem for u_2, we first observe that since $U_2' \to 0$ as $\rho \to \infty$ we must have that

$$\int_0^\infty \left(2\, U_c\, V_c\, V_2 + V_c^2\, U_2 + 2V_c U_1 V_1 + U_c V_1^2\right)\rho\, d\rho = 0\,. \tag{5.19}$$

As a result, the outer problem for u_2 in (5.16b) has no Dirac singularity at $\mathbf{x} = \mathbf{x}_1$. Upon using (5.15) for u_1, we obtain from (5.16b) that the outer problem for u_2 is

$$\Delta u_2 - u_2 = \tau - 2\pi \dot{A} G(\mathbf{x}; \mathbf{x}_1) \,, \quad \text{in } \Omega \,; \qquad \partial_n u_2 = 0 \,, \quad \text{on } \partial\Omega \,. \tag{5.20}$$

To solve (5.20), we decompose u_2 as

$$u_2 = -\tau + 2\pi \dot{A} \mathcal{U}(\mathbf{x}) \,, \tag{5.21}$$

where $\mathcal{U}$ satisfies

$$\Delta \mathcal{U} - \mathcal{U} = -G(\mathbf{x}; \mathbf{x}_1) \,, \quad \text{in } \Omega \,; \qquad \partial_n \mathcal{U} = 0 \,, \quad \text{on } \partial\Omega \,, \tag{5.22}$$

which has the solution

$$\mathcal{U}(\mathbf{x}) = \int_\Omega G(\boldsymbol{\xi}, \mathbf{x}_1) G(\boldsymbol{\xi}, \mathbf{x}) \, d\boldsymbol{\xi} \,. \tag{5.23}$$

The matching condition between the inner and outer solutions is that $\lim_{\mathbf{x} \to \mathbf{x}_1} u_2 = U_{2\infty}$, which yields

$$U_{2\infty} = -\tau + 2\pi \dot{A} \mathcal{U}(\mathbf{x}_1) \,, \qquad \text{where} \qquad \mathcal{U}(\mathbf{x}_1) = \int_\Omega \left[G(\boldsymbol{\xi}, \mathbf{x}_1) \right]^2 d\boldsymbol{\xi} > 0 \,. \tag{5.24}$$

Finally, we substitute (5.24) into (5.18) to obtain the amplitude equation

$$\dot{A} = c_1 \, A^2 + c_2 \, \tau \,, \quad \text{where} \quad c_1 \equiv \frac{\int_0^\infty (V_1^\star - U_1^\star) \, g(\rho) \, \rho \, d\rho}{\int_0^\infty (\partial_S V_c) V_1^\star \, \rho \, d\rho + 2\pi \mathcal{U}(\mathbf{x}_1)} \,, \quad c_2 \equiv \frac{1}{\int_0^\infty (\partial_S V_c) V_1^\star \, \rho \, d\rho + 2\pi \mathcal{U}(\mathbf{x}_1)} \,. \tag{5.25}$$

From a numerical solution to the core and adjoint problems (5.10) and (5.14) at $S = S_c$, respectively, and from a numerical evaluation of $\mathcal{U}(\mathbf{x}_1)$ in (5.24), based on the infinite series for the Green's function derived in Appendix A, we calculate that

$$\int_0^\infty (V_1^\star - U_1^\star) \, g(\rho) \, \rho \, d\rho \approx 11.4825 \,, \qquad \int_0^\infty (\partial_S V_c) V_1^\star \, \rho \, d\rho \approx -8.5064 \,, \qquad \mathcal{U}(\mathbf{x}_1) \approx 1.0033 \,, \tag{5.26}$$

so that $c_1 \approx -5.2138$ and $c_2 \approx -0.45407$ in (5.25).

The solution of the Ricatti equation (5.25) is well-known in the context of ODE problems involving slow passage past a saddle-node point (cf. [9], [6]). From the change of variables

$$A = \alpha w \,, \quad \tau = \beta s \,, \qquad \text{where} \qquad \alpha \equiv -\sqrt[3]{\frac{|c_2|}{c_1^2}} \,, \quad \text{and} \quad \beta \equiv -\frac{1}{\sqrt[3]{|c_1 c_2|}} \,, \tag{5.27}$$

we obtain that the amplitude equation (5.25) reduces to the normal form ODE

$$\frac{dw}{ds} = -w^2 + s \,.$$

By setting $w = \phi'(s)/\phi(s)$, we find that $\phi(s)$ satisfies Airy's equation $\phi'' - s\phi = 0$, which has the general solution $\phi = \text{span}\{\text{Ai}(s), \text{Bi}(s)\}$ in terms of the Airy functions of the first and second kinds. In this way, we get

$$w = \frac{d_0 \, \text{Ai}'(s) + d_1 \, \text{Bi}'(s)}{d_0 \, \text{Ai}(s) + d_1 \, \text{Bi}(s)} \,. \tag{5.28}$$

In terms of these scalings, the rainfall rate a, as obtained from (5.3), (5.9) and (5.27), is $a = a_c - \varepsilon^{2/3}\tau = a_c + \varepsilon^{2/3}|\beta|s$. Moreover, the amplitude of the spot from the inner solution is $V(0) \sim V_c(0) + \varepsilon^{1/3} V_1(0)$, where $V_1(0) = A(\tau)(\partial_S V_c)|_{\rho=0}$ and $A = \alpha w(s)$ from (5.13) and (5.27). In terms of the coefficients c_1 and c_2 in (5.25), we obtain for $\varepsilon \to 0$ that

$$a \sim a_c + \frac{\varepsilon^{2/3} s}{\sqrt[3]{|c_1 c_2|}} \,, \qquad V(0) \sim V_c(0) - \sqrt[3]{\frac{\varepsilon |c_2|}{c_1^2}} \, w(s) \; (\partial_S V_c) \, |_{\rho=0} \,, \tag{5.29}$$

where we have numerically calculated from the core problem (5.10) that $\partial_S V_c|_{\rho=0} = 0.4022 > 0$. We conclude from (5.29) that $a < a_c$ when $s < 0$ and that $a > a_c$ when $s > 0$.

Next, we show that we must set $d_1 = 0$ in (5.28). Since $\mathrm{Ai}(s)$ decays exponentially as $s \to \infty$, while $\mathrm{Bi}(s)$ grows exponentially as $\mathrm{Bi}(s) \sim s^{-1/4}\pi^{-1/2} \exp\left(2s^{\frac{3}{2}}/3\right)$ for $s \to \infty$, we calculate from (5.28) that $w \sim \sqrt{s}$ as $s \to \infty$ when $d_1 \neq 0$. Since $w > 0$, from (5.29) this corresponds to the range $V(0) < V_c(0)$, which contradicts the result that $V(0) > V_c(0)$ when $a > a_c$ (see Fig. 23). Therefore, we must have $d_1 = 0$ in (5.28), and consequently

$$V(0) \sim V_c(0) - \sqrt[3]{\frac{\varepsilon |c_2|}{c_1^2}} \, \frac{\mathrm{Ai}'(s)}{\mathrm{Ai}(s)} \, (\partial_S V_c)\,|_{\rho=0} \,. \tag{5.30}$$

This asymptotic result for the slow passage through the saddle-node bifurcation becomes invalid when s decreases below the first zero of $s_0 \approx -0.23381$ of the Airy function $\mathrm{Ai}(s)$ on the range $s < 0$. The predicted time t_0 characterizing the delayed transition is $t_0 = \varepsilon^{-1/3}\tau_0$, where $\tau_0 = \beta s_0 = -s_0/\sqrt[3]{|c_1 c_2|} > 0$. The corresponding predicted value of the rainfall rate a, labeled by a_0, where this jump transition occurs, and which leads to the annihilation of the spot, is

$$a_0 = a_c - \varepsilon^{2/3}\tau_0 = a_c + \frac{\varepsilon^{2/3} s_0}{\sqrt[3]{|c_1 c_2|}} \approx 13.0757 \,. \tag{5.31}$$

In Fig. 23 we show that this prediction for the delayed transition to spot annihilation compares very favorably with results from a full PDE simulation of (5.2).

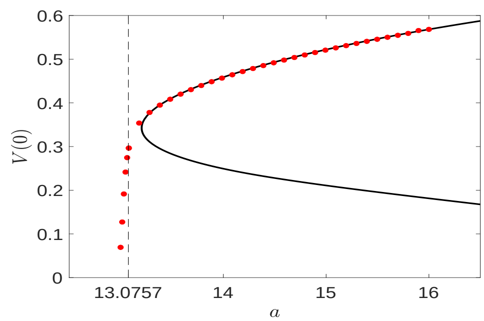

Figure 23: The bifurcation diagram for a quasi steady-state spot centered at the midpoint of the unit square for (5.2). The black solid curve is the spot amplitude $V(0)$ versus the rainfall rate a from the NAS (4.1a). The PDE simulation results with $\varepsilon = 0.02$ and $a(t) = 16 - \varepsilon\, t$, are represented by the red dots. The asymptotic prediction $a_0 \approx 13.0757$ for the jump value of a (dashed vertical line) is seen to compare favorably with the PDE results.

5.3 Delayed spot replication with slowly increasing rainfall

In this subsection we study a delayed transition to spot-splitting for a quasi steady-state spot pattern in the unit square as the rainfall rate is slowly ramped in time as

$$a = a(\tau) = a_0 + \tau \,, \quad \text{with} \quad \tau = \varepsilon t \,, \tag{5.32}$$

beyond the onset of the peanut-splitting threshold labeled by $a = a_c$. In (5.32), a_0 is a constant that is slightly less than a_c. We have chosen the $\mathcal{O}(\varepsilon)$ speed of the ramp to be asymptotically larger than the $\mathcal{O}(\varepsilon^2)$ speed of the slow spot dynamics, so that to leading order the spots remain at their initial locations at $t = 0$ while a is ramped.

Let v_e and u_e denote this quasi steady-state solution, as was constructed in §2, and we introduce a perturbation in the form of the WKBJ ansatz (cf. [1])

$$v = v_e + \exp\left(\psi(\tau)/\varepsilon\right)\phi \,, \qquad u = u_e + \exp\left(\psi(\tau)/\varepsilon\right)\eta \,, \tag{5.33}$$

into (1.1). Upon linearizing, this yields that

$$\varepsilon^2 \Delta\phi - m\phi + 2u_e v_e \phi + v_e^2 \eta = \dot{\psi}\phi \,, \qquad \Delta\eta + H\partial_x \eta - \eta - \varepsilon^{-2}\left(2u_e v_e \phi + v_e^2 \eta\right) = \dot{\psi}\eta \,, \tag{5.34}$$

where $\dot{\psi} = d\psi/d\tau$. As in the linear stability analysis of §3, near the j^{th} spot we let $\phi \sim e^{ik\theta}\Phi_j(\rho)$ and $\eta \sim e^{ik\theta}N_j(\rho)$ for $k \geq 2$, where $\rho = \varepsilon^{-1}\sqrt{m}|\mathbf{x} - \mathbf{x}_j|$, so as to obtain the parametrized eigenvalue problem

$$
\begin{aligned}
&\Delta_\rho \Phi_j - \frac{k^2}{\rho^2}\,\Phi_j - \Phi_j + 2\,U_{j0}V_{j0}\,\Phi_j + V_{j0}^2\,N_j = \frac{\dot{\psi}}{m}\,\Phi_j\,, \quad \rho \geq 0\,, \qquad \Phi_j \to 0 \quad \text{as} \quad \rho \to \infty\,, \\
&\Delta_\rho N_j - \frac{k^2}{\rho^2}\,N_j - 2\,U_{j0}V_{j0}\,\Phi_j - V_{j0}^2\,N_j = 0\,, \quad \rho \geq 0\,, \qquad N_j = \mathcal{O}(\rho^{-k}) \quad \text{as} \quad \rho \to \infty\,.
\end{aligned} \tag{5.35}
$$

Let S_M denote the maximum of the source strengths for the pattern, i.e $S_M = \max_j S_j$, as obtained from the NAS (2.26). We now show how to predict the time delay for the realization of the peanut-splitting instability for this spot as a is slowly ramped above a_c.

Upon comparing (5.35) with (3.4), we conclude that $\dot{\psi} = \lambda$. From the WKBJ ansatz (5.33), the time $\tau = \tau_\star$ for a peanut-splitting instability (for $k = 2$) to be fully realized is given implicitly by

$$
0 = \psi(\tau_\star) = \int_0^{\tau_\star} \lambda\, d\tau = \frac{1}{\varepsilon}\int_{S_{M0}}^{S_{M\star}} \lambda(S_M)\frac{da}{dS_M}\, dS_M\,. \tag{5.36}
$$

Here S_{M0} and $S_{M\star}$ are the source strengths of the M^{th} spot that corresponds to the rainfall rate $a = a_0$ and $a = a_\star$ at times $\tau = 0$ and $\tau = \tau_\star$. To obtain the second equality in (5.36), we applied the change of variable $\tau \to S_M$ with $d\tau = \frac{d\tau}{da}\frac{da}{dS_M}dS_M$. In doing so, we can express λ as a function of S_M, which is readily computed numerically from (3.4) (see Fig. 4 of [13] for a plot of λ versus S_M when $m = 1$). By path-following solutions to the NAS (2.26) we can calculate S_M as a is varied, and then use second order finite differences on a nonuniform grid to approximate da/dS_M. This latter derivative reflects the inverse sensitivity of the maximum spot source strength with respect to the rainfall rate a for a given spatial configuration of spots. Treating (5.36) as a root-finding problem for $S_{M\star}$, we can determine $a_\star$ from the NAS (2.26), from which the predicted delay time is

$$
t_\star = \frac{\tau_\star}{\varepsilon} = \frac{a_\star - a_0}{\varepsilon}\,.
$$

We now illustrate this delayed bifurcation behavior for the special case of a single spot centered at the midpoint $\mathbf{x}_1 = (1/2, 1/2)^T$ of the unit square with $H = 0$ and $m = 1$, and where the rainfall rate is ramped as $a(t) = a_0 + 0.02\,t$ with $a_0 = 34$. With no slope gradient, the spot remains at $\mathbf{x}_1$ as a is ramped. For this one-spot pattern, we let S_1 denote the source strength of the spot, which is determined implicitly from the scalar NAS (4.1a), given by

$$
S_1 + 2\pi\nu S_1 R(\mathbf{x}_1;\mathbf{x}_1) + \nu\chi(S_1) = \nu a\,, \qquad \text{where} \quad \nu = -1/\log\varepsilon\,, \tag{5.37}
$$

with $\varepsilon = 0.02$. Setting $a = a_0 = 24$ in (5.37), the initial spot strength S_{10} at $t = 0$ is calculated as $S_{10} \approx 3.974$. From the linear stability theory of §3 for a static a, the peanut-splitting instability is triggered at $S_1 = \Sigma_2 \approx 4.302$, which from (5.37) corresponds to $a_c \approx 36.347$ at time $t \approx 117.36$. However, by numerically implementing our delayed bifurcation criterion (5.36), we predict that the peanut-spitting instability is only fully realized at $S_1 = S_{1\star} \approx 4.639$, which corresponds to $a_\star \approx 38.736$ and a time $t = t_\star \approx 236.81$.

Next, we verify this prediction for the delayed onset of a peanut-splitting instability for a spot centered at the midpoint of the unit square from full PDE simulations of (1.1) with $H = 0$ and $m = 1$. To do so, we must introduce a metric that measures the deviation from local radial symmetry of the computed PDE solution as time increases. In our algorithm, we select a set of K closed contour lines $\mathcal{T}_1, \ldots, \mathcal{T}_K$ of the PDE solution. For each $\mathcal{T}_i$, we find its least-square fitting circle $\mathcal{C}_i$. Denoting the radius of $\mathcal{C}_i$ by r_i, we define

$$
D_i = \frac{1}{r_i}\max_{\mathbf{x}\in\mathcal{T}_i} ||\mathbf{x} - \text{proj}_{\mathcal{C}_i}(\mathbf{x})||\,,
$$

where $\text{proj}_{\mathcal{C}_i}(\mathbf{x})$ denotes the projection onto the circle $\mathcal{C}_i = \{|\mathbf{x} - \mathbf{x}_1| = r_i\}$, i.e.

$$
\text{proj}_{\mathcal{C}_i}(\mathbf{x}) = \frac{r_i}{|\mathbf{x} - \mathbf{x}_1|}\left(\mathbf{x} - \mathbf{x}_1\right)\,.
$$

The definition of D_i is inspired by the fact that PDE solutions that are nearly radially-symmetric near a spot centered at $\mathbf{x}_1$ have almost circular contour lines locally near $\mathbf{x}_1$. A nearly circular contour line should be very close to its least square fitting circle, which can quantified by the distance between points on the contour and their projection on the fitting circle. However, for a contour line that is small in size, the distance $||\mathbf{x} - \mathrm{cp}(\mathbf{x})||$ can be small regardless of how circular the contour line is. Therefore, we must scale the distance by the radius of the fitting circle. Finally, we define the deviation of the PDE solution from local radial symmetry near the spot by

$$\text{Deviation} = \max_{i=1,\ldots,K} \mathcal{D}_i \,. \tag{5.38}$$

With this metric, in Fig. 24 we show that the asymptotic result for the delayed onset time for the peanut-splitting instability compares very favorably with full PDE simulations of (1.1). Snapshots of the PDE solution showing the delayed spot-splitting behavior are shown in Fig. 25.

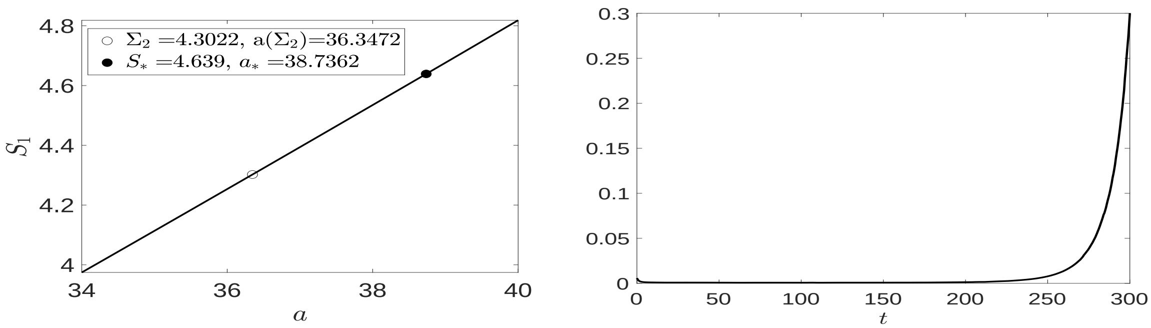

(a) Source strength v.s. a

(b) Deviation from radially symmetry vs. time

Figure 24: Left panel: The source strength S_1 versus the rainfall rate a, computed from the NAS (5.37) for a one spot solution centered at the midpoint $(1/2, 1/2)$ of the unit square with $H = 0$, $\varepsilon = 0.02$, and $m = 1$. The static onset and delayed onset for the peanut-splitting instability are shown by the open and filled circles, respectively. Right panel: The deviation (5.38) from local radial symmetry of the PDE numerical solution computed from (1.1) with the dynamic rainfall rate $a(t) = 34 + 0.02\,t$. The deviation begins to increase very rapidly near our asymptotic prediction $t_\star \approx 236.81$ for the delayed onset time.

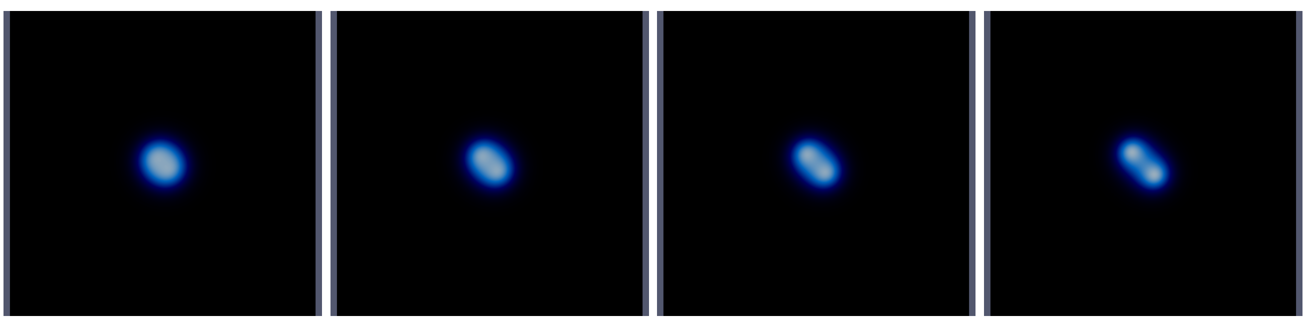

(a) $t = 280$ **(b)** $t = 290$ **(c)** $t = 295$ **(d)** $t = 300$

Figure 25: Snapshots of the full PDE solution of (1.1) with $H = 0$, $m = 1$, $\varepsilon = 0.02$, and $a(t) = 34 + 0.02\,t$ showing a delayed spot-splitting event for a spot centered at the midpoint of the unit square. The results correspond to the deviation metric shown in the right panel of Fig. 24.

5.4 A linearly stable elliptical-shaped spot

We now show numerically that the terrain slope gradient H can lead to a linearly stable elliptical-shaped spot. For various fixed H we use the path-following software *pde2path* [23] to calculate global bifurcation diagrams for a one-spot steady-state of (1.1) in the unit square with $\varepsilon = 0.03$ and $m = 1$, as the rainfall rate a is varied. Since the steady-state location of the spot is on the midline $y = 1/2$, the *pde2path* computation is done in a half square $[0, 1] \times [1/2, 1]$. In Fig. 26, we plot global bifurcation diagrams of the L_2 norm of the v-component in (1.1) versus a for $H = \{0, 0.1, 0.3, 0.5, 0.7, 1.0\}$, with the linearly stable branches indicated by the heavy solid curves. By comparing Fig. 26a with Fig. 26b, we observe that the pitchfork bifurcation when $H = 0$ undergoes a singular perturbation as H is increased to $H = 0.1$, and is transformed into a saddle-node structure. As H is increased further, the saddle-node structure becomes more prominent and the linear stability of a spot is lost at a saddle-node bifurcation. These bifurcation values are given in Table. 1. For $H = 1$, in Fig. 27 we show a zoomed contour plot of some steady-state one-spot solutions at the indicated points in the bifurcation diagram in Fig. 26f, which clearly shows the existence of a linearly stable elliptical-shaped spot (Pt 2 in Fig. 26).

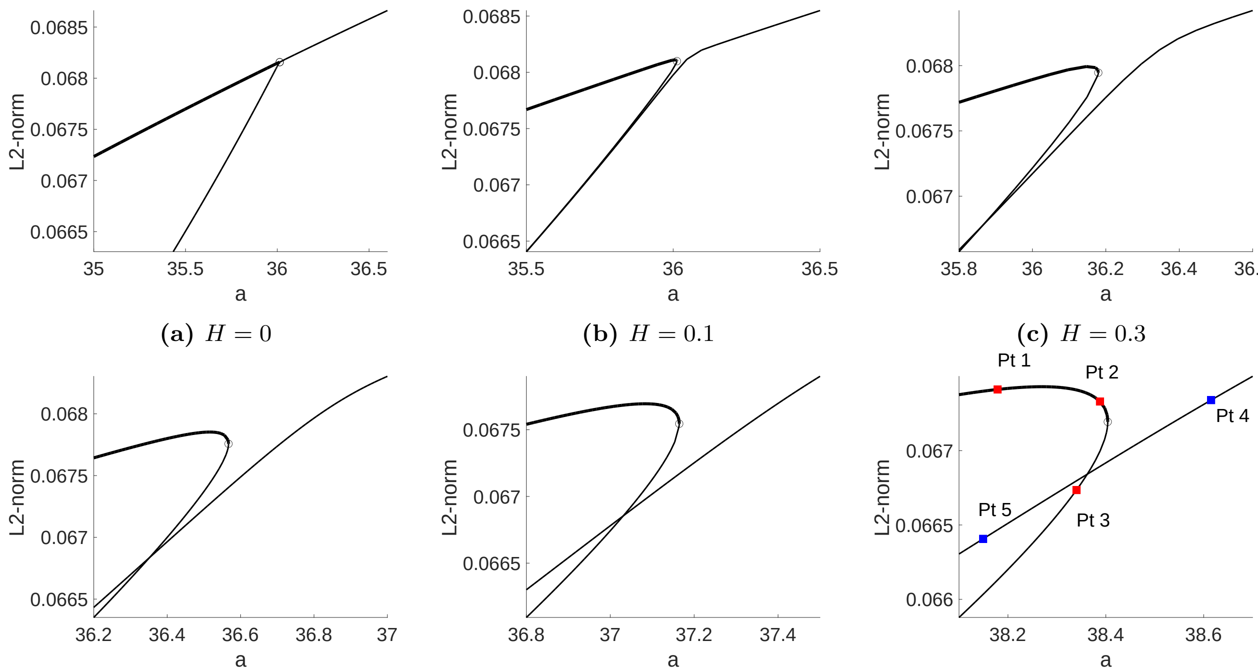

Figure 26: Global bifurcation diagrams for the L_2 norm of the v-component versus the rainfall rate a for a one-spot steady-state solution of (1.1) in the unit square with $\varepsilon = 0.03$ and $m = 1$. A non-zero terrain slope gradient perturbs the pitchfork bifurcation that exists when $H = 0$ into a saddle-node structure.

H	a	S_1
0	36.01	4.5122
0.1	36.01	4.5078
0.3	36.18	4.4988
0.5	36.57	4.4887
0.7	37.16	4.4780
1	38.40	4.4647

Table 1: The bifurcation values in a, as indicated by the open circles in Fig. 26. The corresponding spot source strength S_1 is given.

6 Discussion

We have developed and implemented a hybrid asymptotic-numerical theory to analyze the effects of a constant terrain slope and a time-dependent rainfall rate on 2-D localized vegetation patches for the Klausmeier model (1.1). By using the method of matched asymptotic expansions, we have derived a DAE system that characterizes the slow dynamics of multi-spot equilibria on asymptotically long time scales. The linear stability of these patterns to either spot shape deformations or to competition instabilities that trigger either fully nonlinear spot-splitting or spot-annihilation events, respectively, was analyzed. In the unit square, global bifurcation diagrams for two- and three-spot vertically aligned equilibria of the DAE dynamics were determined in terms of the constant terrain slope

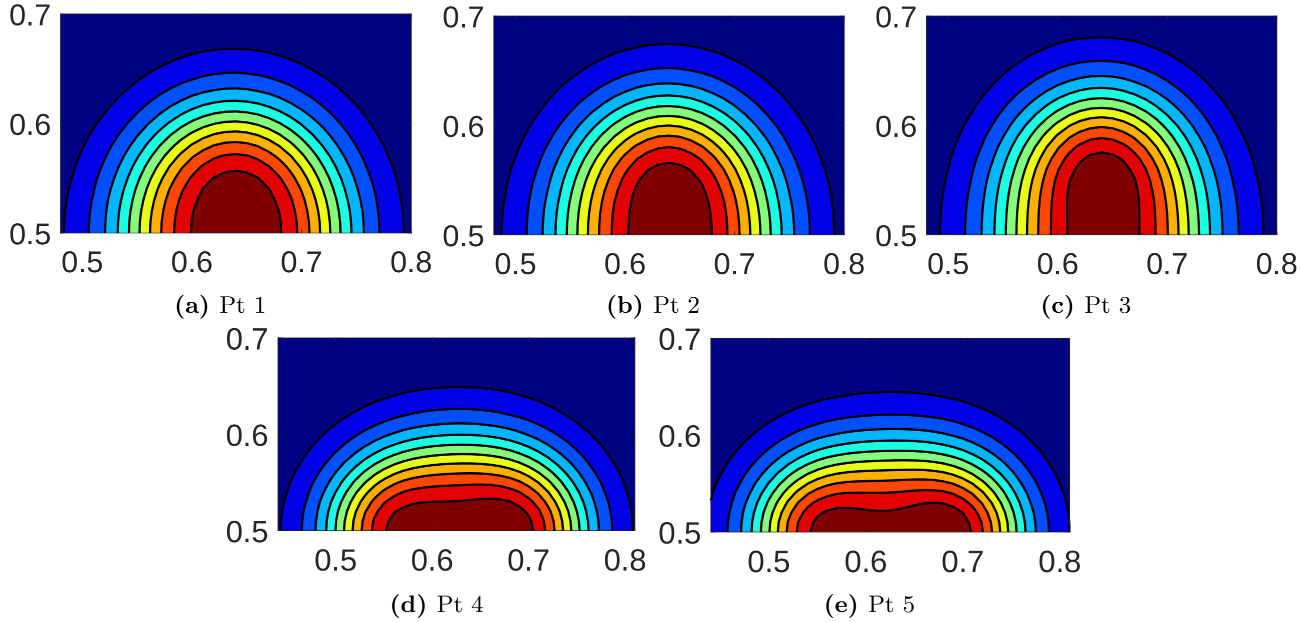

(a) Pt 1 **(b)** Pt 2 **(c)** Pt 3

(d) Pt 4 **(e)** Pt 5

Figure 27: Contour plot (zoomed) of the v-component at the indicated points in the global bifurcation diagram for $H = 1$ in Fig. 26f. (a,b): elongated spot on the linearly stable branch. (c): elongated spot on the unstable branch. (d,e): elongated spots on the isolated unstable branch.

gradient. It was shown that if this slope gradient exceeds a threshold, the DAE dynamics allow for a linearly stable two-spot vertically aligned steady-state with spots located on the uphill side of the terrain gradient.

When the rainfall rate is slowly decreasing in time, competition instabilities for multi-spot quasi-equilibria can be triggered at certain times during the slow dynamics of multi-spot quasi-equilibria. To study these sudden transitions, we have augmented the DAE system for slow spot dynamics with a zero-eigenvalue crossing criterion, based on the linear stability analysis, that accurately predicts the onset of spot-annihilation events. With this algorithm, the DAE dynamics for the spot locations can be continued in time after sudden spot-annihilation events, until a final steady-state pattern is obtained. The spot trajectories from our augmented DAE algorithm, both before and after spot-annihilation events, were favorably compared with corresponding full numerical results computed from the Klausmeier PDE model (1.1). For a one-spot pattern in the unit square we have also analyzed the delayed bifurcation behavior associated with either competition or peanut-splitting instabilities that can occur from either a slowly decreasing or a slowly increasing rainfall rate, respectively.

We now briefly discuss a few specific problems that warrant further investigation. We have shown that a three-spot vertically aligned pattern in the unit square is unstable as a steady-state of the DAE dynamics. By increasing the width of the domain it would be interesting to determine threshold values on the domain width for which three or more vertically aligned spots can be stabilized. A second extension would be to analyze spot dynamics for multi-spot quasi-equilibria in a rectangle in the presence of a spatially varying terrain gradient of the form $H = H(x)$. In [3], it has been shown the convexity of $H(x)$ can determine whether a one-dimensional spike would migrate uphill or downhill the slope gradient. It would be interesting to analyze whether the convexity of $H(x)$ has a similar effect on spot dynamics in a 2-D context. For this extension, the infinite series solution for the Green's function constructed in Appendix A for a uniform terrain slope no longer applies, and the general framework developed in [21], based on microlocal analysis, would be needed for efficiently computing the required Green's function. A third open problem is to theoretically predict the existence of a linearly stable non-radially symmetric spot solution, as was shown numerically in Fig. 26 and Fig. 27. The pitchfork bifurcation structure for a vanishing slope gradient $H = 0$ was observed to be structurally unstable to small perturbations in $H > 0$. It would be interesting to characterize this singular perturbation of the bifurcation through a weakly nonlinear analysis. Finally, it would be interesting to perform a weakly nonlinear analysis on the spot amplitudes to show that a linear competition instability is subcritical, and triggers a spot-annihilation event. In our DAE simulation algorithm it was implicitly assumed that the onset of a linear competition instability does indeed forecast a nonlinear spot-annihilation event.

References

[1] S. M. Baer, T. Erneux, and J. Rinzel, *The slow passage through a hopf bifurcation: delay, memory effects, and resonance*, SIAM J. Appl. Math., 49 (1989), pp. 55–71.

[2] R. Bastiaansen, P. Carter, and A. Doelman, *Stable planar vegetation stripe patterns on sloped terrain in dryland ecosystems*, Nonlineariy, 32 (2019), pp. 2759–2814.

[3] R. Bastiaansen and A. Doelman, *The dynamics of disappearing pulses in a singularly perturbed reaction–diffusion system with parameters that vary in time and space*, Physica D, 388 (2019), pp. 45–72.

[4] W. Chen and M. J. Ward, *The stability and dynamics of localized spot patterns in the two-dimensional Gray-Scott model*, SIAM J. Appl. Dyn. Sys., 10 (2011), pp. 582–666.

[5] Y. Chen, T. Kolokolnikov, J. Tzou, and C. Gai, *Patterned vegetation, tipping points, and the rate of climate change*, Europ. J. Appl. Math., 26 (2015), pp. 945–958.

[6] T. Erneux and P. Mandel, *Imperfect bifurcation with a slowly varying control parameter*, SIAM J. Appl. Math., 46 (1986), pp. 1–15.

[7] P. Gandhi, L. Werner, S. Iams, K. Gowda, and M. Silber, *A topographic mechanism for arcing of dryland vegetation bands*, J. Roy. Soc. Interface, 15 (2018), p. 20180508.

[8] E. Gilad, J. von Hardenberg, A. Provenzale, M. Shachak, and E. Meron, *Ecosystem engineers: from pattern formation to habitat creation*, Phys. Rev. Lett., 93 (2004), p. 098105.

[9] R. Haberman, *Slowly varying jump and transition phenomena associated with algebraic bifurcation problems*, SIAM J. Appl. Math., 37 (1979), pp. 69–106.

[10] C. A. Klausmeier, *Regular and irregular patterns in semiarid vegetation*, Science, 284 (1999), pp. 1826–1828.

[11] K. Knopp, *Theory and application of infinite series*, Dover Books on Mathematics, Dover Publications, 2013.

[12] T. Kolokolnikov, M. Ward, J. Tzou, and J. Wei, *Stabilizing a homoclinic stripe*, Phil. Trans. Roy. Soc. A: Math., Phys. and Eng. Sci., 376 (2018), p. 20180110.

[13] T. Kolokolnikov, M. J. Ward, and J. Wei, *Spot self-replication and dynamics for the Schnakenburg model in a two-dimensional domain*, J. Nonlinear Science, 19 (2009), pp. 1–56.

[14] P. Mandel and T. Erneux, *The slow passage through a steady bifurcation: delay and memory effects*, J. Stat. Phys., 48 (1987), pp. 1059–1070.

[15] The Mathworks, Inc., *MATLAB version 9.4.0.813654 (R2018a)*, Natick, Massachusetts, 2018.

[16] E. Meron, *Modeling dryland landscapes*, Mathematical Modelling of Natural Phenomena, 6 (2011), pp. 163–187.

[17] ——, *Nonlinear physics of ecosystems*, CRC Press, 2015.

[18] L. Sewalt and A. Doelman, *Spatially periodic multipulse patterns in a generalized Klausmeier–Gray–Scott model*, SIAM J. Appl. Dyn. Sys., 16 (2017), pp. 1113–1163.

[19] E. Siero, A. Doelman, M. Eppinga, J. D. Rademacher, M. Rietkerk, and K. Siteur, *Striped pattern selection by advective reaction-diffusion systems: Resilience of banded vegetation on slopes*, Chaos: An Interdisciplinary J. of Nonl. Sci., 25 (2015), p. 036411.

[20] J. C. Tzou and L. Tzou, *Spot patterns of the Schnakenberg reaction-diffusion system on a curved torus*, Nonlinearity, 33 (2019), pp. 643–674.

[21] J. C. Tzou and L. Tzou, *Analysis of spot patterns on a coordinate-invariant model for vegetation on a curved terrain*, SIAM J. Appl. Dyn. Sys., 19 (2020), pp. 2500–2529.

[22] J. C. Tzou, M. J. Ward, and T. Kolokolnikov, *Slowly varying control parameters, delayed bifurcations, and the stability of spikes in reaction-diffusion systems*, Physica D, 290 (2015), pp. 24–43.

[23] H. Uecker, D. Wetzel, and J. D. Rademacher, *pde2path-a matlab package for continuation and bifurcation in 2d elliptic systems*, Numerical Mathematics: Theory, Methods and Applications, 7 (2014), pp. 58–106.

[24] S. van der Stelt, A. Doelman, G. Hek, and J. D. Rademacher, *Rise and fall of periodic patterns for a generalized Klausmeier–Gray–Scott model*, J. Nonlinear Science, 23 (2013), pp. 39–95.

[25] J. von Hardenberg, E. Meron, M. Shachak, and Y. Zarmi, *Diversity of vegetation patterns and*

desertification, Phys. Rev. Lett., 87 (2001), p. 198101.

[26] T. Wong and M. J. Ward, *Weakly nonlinear analysis of peanut-shaped deformations for localized spots of singularly perturbed reaction-diffusion systems*, SIAM J. Appl. Dyn. Sys., 19 (2020), pp. 2030–2058.

[27] ——, *Spot patterns in the 2-d Schnakenberg model with localized heterogeneities*, Studies in Appl. Math., (2021).

[28] Y. R. Zelnik, E. Meron, and G. Bel, *Gradual regime shifts in fairy circles*, Proc. Nat. Acad. of Sci., 112 (2015), pp. 12327–12331.

A Series solution for the Green's function

In this appendix we derive computationally tractable formulae for computing the Green's function and its regular part satisfying (3.9) in the rectangular domain $\Omega = \{(x,y)\,|\,0<x<l\,,\,0<y<h\}$.

A.1 Fourier cosine expansion

We write $\mathbf{x}=(x,y)^T$ and $\mathbf{x}_0=(x_0,y_0)^T$, and assume that $H>0$. We consider the eigenvalue-dependent Green's function of (3.9) in the rectangle Ω, and set

$$G_\lambda(\mathbf{x};\mathbf{x}_0) = e^{K(x_0-x)} F_\lambda(\mathbf{x};\mathbf{x}_0)\,, \qquad \text{where} \qquad K \equiv H/2\,, \tag{A.1}$$

so that $F_\lambda(\mathbf{x};\mathbf{x}_0)$ satisfies

$$\Delta F_\lambda - (1+\lambda+K^2)F_\lambda = -\delta(\mathbf{x}-\mathbf{x}_0) \quad \text{in} \quad \Omega\,, \tag{A.2a}$$
$$\partial_x F_\lambda - K F_\lambda = 0 \quad \text{on} \quad x=0,l\,; \qquad \partial_y F_\lambda = 0 \quad \text{on } y=0,h\,. \tag{A.2b}$$

As a result of the Neumann boundary conditions at $y=0,h$, we expand F_λ in a Fourier cosine expansion as

$$F_\lambda = A_0(x) + \sum_{n=1}^{\infty} A_n(x)\cos\left(\frac{n\pi y}{h}\right)\,. \tag{A.3}$$

We readily derive that the coefficients $A_n(x)$ satisfy

$$A_n'' - \alpha_n^2 A_n = \begin{cases} -h^{-1}\delta(x-x_0)\,, & \text{for } n=0\,, \\ -2h^{-1}\cos\left(\frac{n\pi y_0}{h}\right)\,\delta(x-x_0)\,, & \text{for } n>0\,, \end{cases} \qquad \text{with} \qquad A_n' = K A_n\,, \quad \text{at} \quad x=0,l\,, \tag{A.4}$$

where α_n is defined by

$$\alpha_n = \sqrt{1+\lambda+K^2+\frac{n^2\pi^2}{h^2}}\,, \quad \text{for} \quad n\geq 0\,. \tag{A.5}$$

For some undetermined constant k_n, the solution to (A.4) is

$$A_n = k_n\Big[(\alpha_n+K)e^{\alpha_n(x_>-l)} + (\alpha_n-K)e^{\alpha_n(l-x_>)}\Big]\cdot\Big[(\alpha_n+K)e^{\alpha_n x_<} + (\alpha_n-K)e^{-\alpha_n x_<}\Big]\,, \tag{A.6}$$

where we have defined $x_> = \max(x,x_0)$ and $x_< = \min(x,x_0)$. By using the identities $x_> + x_< = x+x_0$ and $x_> - x_< = |x-x_0|$, we conclude that

$$A_n = k_n\Big[(\alpha_n+K)^2 e^{\alpha_n(x+x_0-l)} + (\alpha_n^2-K^2)\left(e^{\alpha_n(|x-x_0|-l)} + e^{\alpha_n(l-|x-x_0|)}\right) + (\alpha_n-K)^2 e^{\alpha_n(l-x-x_0)}\Big]\,. \tag{A.7}$$

The jump conditions for (A.4) are

$$A_n'(x_0^+) - A_n'(x_0^-) = \begin{cases} -h^{-1}\,, & \text{for } n=0\,, \\ -2h^{-1}\cos\left(\dfrac{n\pi y_0}{h}\right)\,, & \text{for } n>0\,. \end{cases} \tag{A.8}$$

We readily calculate from (A.7) that

$$A_n'(x_0^{\pm}) = \alpha_n k_n \left[(\alpha_n + K)^2 e^{\alpha_n(2x_0-l)} \mp (\alpha_n^2 - K^2)(e^{\alpha_n l} - e^{-\alpha_n l}) - (\alpha_n - K)^2 e^{\alpha_n(l-2x_0)}\right],$$

so that the jump in the derivative is

$$A_n'(x_0^+) - A_n'(x_0^-) = -2\alpha_n k_n (\alpha_n^2 - K^2)\,(e^{\alpha_n l} - e^{-\alpha_n l})\,. \tag{A.9}$$

Comparing (A.9) with (A.8), we determime k_n as

$$k_n = \frac{\cos(\frac{n\pi y_0}{h})}{h\sigma_n \alpha_n(\alpha_n^2 - K^2)(e^{\alpha_n l} - e^{-\alpha_n l})}\,, \qquad \text{where} \qquad \sigma_n \equiv \begin{cases} 2\,, & \text{for } n = 0\,, \\ 1\,, & \text{for } n > 0\,. \end{cases} \tag{A.10}$$

We then substitute (A.10) into (A.7) to get for $n \geq 0$ that

$$\begin{aligned} A_n =& \frac{\cos\left(\frac{n\pi y_0}{h}\right)}{h\sigma_n\alpha_n\left(1 - \frac{K^2}{\alpha_n^2}\right)(1 - e^{-2\alpha_n l})}\left[\left(1 + \frac{K}{\alpha_n}\right)^2 e^{\alpha_n(x+x_0-2l)} + \right. \\ & \left.\left(1 - \frac{K^2}{\alpha_n^2}\right)\left(e^{\alpha_n(|x-x_0|-2l)} + e^{-\alpha_n|x-x_0|}\right) + \left(1 - \frac{K}{\alpha_n}\right)^2 e^{-\alpha_n(x+x_0)}\right]. \end{aligned} \tag{A.11}$$

In this way, the Fourier cosine expansion of F_λ is given by (A.3) where the coefficients $A_n(x)$ are given explicitly in (A.11). However, since this expansion of the Green's function diverges at $\mathbf{x} = \mathbf{x}_0$, it exhibits poor convergence properties in the domain. As such, we now show how to extract the logarithmic singularity from the infinite sum so as to obtain a rapidly converging infinite series representation for F_λ and its regular part.

A.2 Accelerating convergence of the infinite series solution

We proceed by isolating the singular part of the infinite series (A.3) by first introducing the decomposition,

$$F_\lambda = A_0 + \mathcal{S}_1 + \mathcal{S}_2\,, \tag{A.12}$$

where $\mathcal{S}_1$ and $\mathcal{S}_2$ are defined by

$$\begin{aligned} \mathcal{S}_1 \equiv \sum_{n=1}^{\infty} \frac{\cos\left(\frac{n\pi y_0}{h}\right)\cos\left(\frac{n\pi y}{h}\right)}{h\alpha_n\left(1 - \frac{K^2}{\alpha_n^2}\right)(1 - e^{-2\alpha_n l})} & \left[\left(1 + \frac{K}{\alpha_n}\right)^2 e^{\alpha_n(x+x_0-2l)} + \left(1 - \frac{K^2}{\alpha_n^2}\right) e^{\alpha_n(|x-x_0|-2l)}\right. \\ & \left. + \left(1 - \frac{K}{\alpha_n}\right)^2 e^{-\alpha_n(x+x_0)}\right], \end{aligned} \tag{A.13}$$

and

$$\mathcal{S}_2 \equiv \sum_{n=1}^{\infty} f(n)\cos\left(\frac{n\pi y_0}{h}\right)\cos\left(\frac{n\pi y}{h}\right)\,, \qquad \text{where} \qquad f(n) \equiv \frac{e^{-\alpha_n|x-x_0|}}{h\,\alpha_n\,(1 - e^{-2\alpha_n l})}\,. \tag{A.14}$$

The series $\mathcal{S}_1$ converges rapidly, provided that both x, x_0 are not too close to zero or to $l = \mathcal{O}(1)$. In contrast, the series $\mathcal{S}_2$ diverges when $\mathbf{x} = \mathbf{x}_0$ since it contains the logarithmic singularity of the Green's function. Therefore, we identify $\mathcal{S}_2$ as the slowly converging component.

To extract the divergent behavior we apply Kummer's transformation (cf. [11]), where we seek an asymptotic approximation $f_\sigma(n)$ to $f(n)$ such that

$$\mathcal{S}_2 = \sum_{n=1}^{\infty}\left[f(n) - f_\sigma(n)\right]\cos\left(\frac{n\pi y_0}{h}\right)\cos\left(\frac{n\pi y}{h}\right) + \sum_{n=1}^{\infty} f_\sigma(n)\cos\left(\frac{n\pi y_0}{h}\right)\cos\left(\frac{n\pi y}{h}\right)\,, \tag{A.15}$$

where $f(n)/f_\sigma(n)$ tends to a constant as $n \to \infty$, but where the infinite series involving f_σ can be summed explicitly.

To this end, we first calculate using the Binomial approximation on (A.5) that for $n \gg 1$

$$\alpha_n = \frac{n\pi}{h} + \frac{h(1+\lambda+K^2)}{2n\pi} - \frac{h^3(1+\lambda+K^2)^2}{8n^3\pi^3} + \mathcal{O}(n^{-5}) \,. \tag{A.16}$$

In this way, we derive for any s that as $n \to \infty$,

$$e^{-\alpha_n s} = e^{-\frac{n\pi s}{h}} \left[1 - \frac{h(1+\lambda+K^2)s}{2n\pi} + \frac{h^2(1+\lambda+K^2)^2 s^2}{8n^2\pi^2} + \mathcal{O}(n^{-3}s)\right] . \tag{A.17}$$

By using (A.17), we conclude that

$$1 - e^{-2\alpha_n l} = 1 + \mathcal{O}\left(e^{-\frac{2n\pi l}{h}}\right) , \tag{A.18}$$

and upon setting $s = |x - x_0|$ in (A.17), we get

$$e^{-\alpha_n|x-x_0|} = e^{-\frac{n\pi|x-x_0|}{h}} \left[1 - \frac{h(1+\lambda+K^2)|x-x_0|}{2n\pi} + \frac{h^2(1+\lambda+K^2)^2|x-x_0|^2}{8n^2\pi^2} + \mathcal{O}\left(n^{-3}|x-x_0|\right)\right] . \tag{A.19}$$

By combining the estimates (A.16), (A.17) and (A.18), we conclude that

$$\begin{aligned} f(n) = e^{-\frac{n\pi|x-x_0|}{h}} \Bigg\{ & \frac{1}{n\pi} - \frac{h(1+\lambda+K^2)|x-x_0|}{2n^2\pi^2} + \frac{h^2(1+\lambda+K^2)}{n^3\pi^3}\left[\frac{(1+\lambda+K^2)|x-x_0|^2}{8} - \frac{1}{2}\right] \\ & + \mathcal{O}\left(n^{-4}|x-x_0|\right) + \mathcal{O}\left(n^{-5}\right) \Bigg\} . \end{aligned} \tag{A.20}$$

In this way, we have identified that an asymptotic approximation to $f(n)$ with the same large n behavior is

$$f_\sigma(n) = e^{-\frac{n\pi|x-x_0|}{h}} \left\{\frac{1}{n\pi} - \frac{h(1+\lambda+K^2)|x-x_0|}{2n^2\pi^2} + \frac{h^2(1+\lambda+K^2)}{n^3\pi^3}\left[\frac{(1+\lambda+K^2)|x-x_0|^2}{8} - \frac{1}{2}\right]\right\} . \tag{A.21}$$

With the error estimate in (A.20), the choice of $f_\sigma(n)$ given by (A.21) yields the rapid convergence of the residual series $\sum_{n=1}^{\infty} [f(n) - f_\sigma(n)] \cos\left(\frac{n\pi y_0}{h}\right) \cos\left(\frac{n\pi y}{h}\right)$ in (A.15).

Next, we express the sum $\sum_{n=1}^{\infty} f_\sigma(n) \cos\left(\frac{n\pi y_0}{h}\right) \cos\left(\frac{n\pi y}{h}\right)$ in terms of the polylogarithm function Li_s, defined by

$$\mathrm{Li}_1(z) \equiv -\log(1-z) \,, \qquad \mathrm{Li}_s(z) \equiv \sum_{n=1}^{\infty} \frac{z^n}{n^s} \,,$$

which is readily computed as a special function in Matlab [15]. We first observe that

$$\cos\left(\frac{n\pi y_0}{h}\right)\cos\left(\frac{n\pi y}{h}\right) = \frac{1}{4}\left[e^{\frac{in\pi(y+y_0)}{h}} + e^{\frac{-in\pi(y+y_0)}{h}} + e^{\frac{in\pi(y-y_0)}{h}} + e^{\frac{in\pi(y_0-y)}{h}}\right] , \tag{A.22}$$

and so by using this identity, and by defining

$$z_\pm \equiv -|x-x_0| + i(y \pm y_0) \,, \quad \mathcal{L}_s(z_+, z_-) \equiv \frac{1}{4}\left[\mathrm{Li}_s\left(e^{\frac{\pi z_+}{h}}\right) + \mathrm{Li}_s\left(e^{\frac{\pi z_+^\star}{h}}\right) + \mathrm{Li}_s\left(e^{\frac{\pi z_-}{h}}\right) + \mathrm{Li}_s\left(e^{\frac{\pi z_-^\star}{h}}\right)\right] , \tag{A.23}$$

where the $\star$ denotes conjugation, we obtain that

$$\sum_{n=1}^{\infty} \frac{e^{-\frac{n\pi|x-x_0|}{h}}}{n^s} \cos\left(\frac{n\pi y_0}{h}\right)\cos\left(\frac{n\pi y}{h}\right) = \frac{1}{4}\sum_{n=1}^{\infty}\left(\frac{e^{\frac{n\pi z_+}{h}}}{n^s} + \frac{e^{\frac{n\pi z_+^\star}{h}}}{n^s} + \frac{e^{\frac{n\pi z_-}{h}}}{n^s} + \frac{e^{\frac{n\pi z_-^\star}{h}}}{n^s}\right) = \mathcal{L}_s(z_+, z_-) \,. \tag{A.24}$$

Upon summing (A.21) by using the identity (A.24) we obtain that

$$\begin{aligned} \sum_{n=1}^{\infty} f_\sigma(n)\cos\left(\frac{n\pi y_0}{h}\right)\cos\left(\frac{n\pi y}{h}\right) = & \frac{1}{\pi}\mathcal{L}_1(z_+, z_-) - \frac{h(1+\lambda+K^2)|x-x_0|}{2\pi^2}\mathcal{L}_2(z_+, z_-) \\ & + \frac{h^2(1+\lambda+K^2)}{\pi^3}\left[\frac{(1+\lambda+K^2)|x-x_0|^2}{8} - \frac{1}{2}\right]\mathcal{L}_3(z_+, z_-) \,. \end{aligned} \tag{A.25}$$

Numerical values of polylogarithm functions, and therefore (A.25) can be computed with high accuracy and efficiency with Matlab [15]. In conclusion, the numerical evaluation of $F_\lambda(\mathbf{x};\mathbf{x}_0)$ (assuming $\mathbf{x}\neq\mathbf{x}_0$) as given in the decomposition (A.12) can be numerically computed efficiently as follows. Firstly, A_0 is obtained by setting $n=0$ in (A.11). Secondly, $\mathcal{S}_1$ can be approximated by a finite sum of the infinite series in (A.13). Finally, as given in (A.15), we decompose $\mathcal{S}_2$ into the sum of two infinite series. The first series can be approximated by a finite sum using the definitions of $f(n)$ and $f_\sigma(n)$ that are given in (A.14) and (A.21), respectively. The second infinite series is calculated by evaluating some polylogarithmic functions as shown in (A.25).

A.3 Isolating the logarithmic singularity from the series solution

The regular part $R_\lambda(\mathbf{x}_0;\mathbf{x}_0)$ of G_λ is defined in (3.9). By letting $\mathbf{x}\to\mathbf{x}_0$ in (A.1), we obtain equivalently that

$$F_\lambda(\mathbf{x};\mathbf{x}_0) = -\frac{1}{2\pi}\log|\mathbf{x}-\mathbf{x}_0| + R_\lambda(\mathbf{x}_0;\mathbf{x}_0) + o(1)\,, \quad \text{as} \quad \mathbf{x}\to\mathbf{x}_0\,. \tag{A.26}$$

We now derive a computationally efficient formula for $R_\lambda(\mathbf{x}_0;\mathbf{x}_0)$.

For $\mathbf{x}\to\mathbf{x}_0$, we obtain from (A.23) that

$$z_+ \to z_+^0 \equiv 2iy_0\,, \qquad z_- \to z_-^0 \equiv 0\,. \tag{A.27}$$

Therefore, for any $s\geq 2$, we have from (A.23) that

$$\mathcal{L}_s(z_+,z_-) \to \mathcal{L}_s(z_+^0,z_-^0)\,, \quad \text{as} \quad \mathbf{x}\to\mathbf{x}_0\,. \tag{A.28}$$

Based on the results that

$$\left[\mathrm{Li}_1\left(e^{\frac{\pi z_-}{h}}\right) + \mathrm{Li}_1\left(e^{\frac{\pi z_-^\star}{h}}\right)\right] = -\log\left|1-e^{\frac{\pi z_-}{h}}\right|^2\,, \tag{A.29}$$

and

$$\left|1-e^{\frac{\pi z_-}{h}}\right|^2 \to \frac{\pi^2}{h^2}\left[(x-x_0)^2+(y-y_0)^2\right]\,, \quad \text{as} \quad \mathbf{x}\to\mathbf{x}_0\,, \tag{A.30}$$

we conclude from (A.23) that

$$\mathcal{L}_1(z_+,z_-) = \frac{1}{4}\left[\mathrm{Li}_1\left(e^{\frac{\pi z_+}{h}}\right) + \mathrm{Li}_1\left(e^{\frac{\pi z_+^\star}{h}}\right)\right] - \frac{1}{4}\log\left|1-e^{\frac{\pi z_-}{h}}\right|^2\,, \tag{A.31}$$

has the limiting behavior

$$\mathcal{L}_1(z_+,z_-) \to \frac{1}{4}\left[\mathrm{Li}_1\left(e^{\frac{\pi z_+^0}{h}}\right) + \mathrm{Li}_1\left(e^{\frac{\pi (z_+^0)^\star}{h}}\right)\right] - \frac{1}{2}\log|\mathbf{x}-\mathbf{x}_0| - \frac{1}{2}\log\left(\frac{\pi}{h}\right) + o(1)\,, \quad \text{as} \quad \mathbf{x}\to\mathbf{x}_0\,. \tag{A.32}$$

Combining the results (A.28) and (A.32) with

$$f(n)\to f_0(n) \equiv \frac{1}{h\alpha_n(1-e^{-2\alpha_n l})}\,, \qquad f_\sigma(n)\to f_{\sigma 0}(n) \equiv \left[\frac{1}{n\pi} - \frac{h^2(1+\lambda+K^2)}{2n^3\pi^3}\right]\,, \tag{A.33}$$

as $\mathbf{x}\to\mathbf{x}_0$, we derive from (A.15) and (A.25) that

$$\mathcal{S}_2 \to -\frac{1}{2\pi}\log|\mathbf{x}-\mathbf{x}_0| - \frac{1}{2\pi}\log\left(\frac{\pi}{h}\right) + T_2 + o(1)\,, \quad \text{as} \quad \mathbf{x}\to\mathbf{x}_0\,, \tag{A.34}$$

where we have defined T_2 by

$$T_2 \equiv \sum_{n=1}^{\infty}\left[f_0(n)-f_{\sigma 0}(n)\right]\cos^2\left(\frac{n\pi y_0}{h}\right) + \frac{1}{4\pi}\left[\mathrm{Li}_1\left(e^{\frac{\pi z_+^0}{h}}\right) + \mathrm{Li}_1\left(e^{\frac{\pi (z_+^0)^\star}{h}}\right)\right] - \frac{h^2(1+\lambda+K^2)}{2\pi^3}\,\mathcal{L}_3(z_+^0,z_-^0)\,. \tag{A.35}$$

Then, by letting $\mathbf{x}\to\mathbf{x}_0$ in the decomposition (A.12) of F_λ, we use (A.34) and (A.13) to obtain

$$F_\lambda = A_0 + \mathcal{S}_1 + \mathcal{S}_2 \sim -\frac{1}{2\pi}\log|\mathbf{x}-\mathbf{x}_0| - \frac{1}{2\pi}\log\left(\frac{\pi}{h}\right) + A_{00} + T_1 + T_2 + o(1)\,, \quad \text{as} \quad \mathbf{x}\to\mathbf{x}_0\,, \tag{A.36}$$

where A_{00} and T_1 are the limiting behaviors of A_0 and $\mathcal{S}_1$ as $\mathbf{x} \to \mathbf{x}_0$ given by

$$A_0 \to A_{00} \equiv \frac{(1+\frac{K}{\alpha_0})^2 e^{2\alpha_0(x_0-l)} + (1-\frac{K^2}{\alpha_0^2})(1+e^{-2\alpha_0 l}) + (1-\frac{K}{\alpha_0})^2 e^{-2\alpha_0 x_0}}{2h\alpha_0(1-\frac{K^2}{\alpha_0^2})(1-e^{-2\alpha_0 l})}\,, \tag{A.37a}$$

$$\mathcal{S}_1 \to T_1 \equiv \sum_{n=1}^{\infty} \frac{(1+\frac{K}{\alpha_n})^2 e^{2\alpha_n(x_0-l)} + (1-\frac{K^2}{\alpha_n^2})e^{-2\alpha_n l} + (1-\frac{K}{\alpha_n})^2 e^{-2\alpha_n x_0}}{h\alpha_n(1-\frac{K^2}{\alpha_n^2})(1-e^{-2\alpha_n l})} \cos^2\left(\frac{n\pi y_0}{h}\right)\,. \tag{A.37b}$$

By enforcing that the limiting behavior in (A.26) agrees with that given in (A.36), we identify the regular part as

$$R_\lambda(\mathbf{x}_0;\mathbf{x}_0) = -\frac{1}{2\pi}\log\left(\frac{\pi}{h}\right) + A_{00} + T_1 + T_2\,, \tag{A.38}$$

where T_2, A_{00} and T_1 are defined in (A.35) and (A.37). We remark that upon setting $\lambda = 0$ in (A.38), we also obtain a computationally efficient formula for $R(\mathbf{x}_0;\mathbf{x}_0)$, as defined in (2.20), which is needed in the NAS (2.26) that arises from the asymptotic construction of quasi-equilibrium multi-spot patterns.

B Linear stability of the DAE equilibria

In this appendix we derive a criterion to determine the linear stability of equilibria to the DAE system (2.30). For convenience, we denote the DAE system (2.30) subject to the nonlinear constraints as

$$\dot{\mathbf{w}} = \mathbf{F}(\mathbf{w},\mathbf{s})\,, \quad \text{and} \quad \mathbf{G}(\mathbf{w},\mathbf{s}) = \mathbf{0}\,, \tag{B.1}$$

where $\mathbf{w} \equiv (x_1, y_1, \ldots, x_N, y_N)^T \in \mathbb{R}^{2N}$ and $\mathbf{s} \equiv (S_1, \ldots, S_N)^T \in \mathbb{R}^N$. Given an N-spot equilibrium, we define

$$\mathbf{w}_e \equiv (x_{1e}, y_{1e}, \ldots, x_{Ne}, y_{Ne})^T \in \mathbb{R}^{2N}\,, \qquad \mathbf{s}_e \equiv (S_{1e}, \ldots, S_{Ne})^T \in \mathbb{R}^N\,, \tag{B.2}$$

where (x_{je}, y_{je}) and S_{je} is the steady-state location and the source strength of the j^{th} spot, so that $\mathbf{F}(\mathbf{w}_e, \mathbf{s}_e) = \mathbf{0}$ and $\mathbf{G}(\mathbf{w}_e, \mathbf{s}_e) = \mathbf{0}$. Then, we linearize (B.1) by substituting $\mathbf{w} = \mathbf{w}_e + \boldsymbol{\xi}$ and $\mathbf{s} = \mathbf{s}_e + \boldsymbol{\eta}$, which yields

$$\dot{\boldsymbol{\xi}} = D_{\mathbf{w}}F_e \cdot \boldsymbol{\xi} + D_{\mathbf{s}}F_e \cdot \boldsymbol{\eta}\,, \qquad 0 = D_{\mathbf{w}}G_e \cdot \boldsymbol{\xi} + D_{\mathbf{s}}G_e \cdot \boldsymbol{\eta}\,. \tag{B.3}$$

Here, $D_{\mathbf{w}}F_e$ ($D_{\mathbf{w}}G_e$) and $D_{\mathbf{s}}F_e$ ($D_{\mathbf{s}}G_e$) represent the Jacobian matrix of F (G) with respect to $\mathbf{w}$ and $\mathbf{s}$, respectively, evaluated at $\mathbf{w} = \mathbf{w}_e$ and $\mathbf{s} = \mathbf{s}_e$. By combining the two equations in (B.3), we derive that

$$\dot{\boldsymbol{\xi}} = \mathcal{Q}\boldsymbol{\xi}\,, \qquad \text{where} \qquad \mathcal{Q} = \mathcal{Q}(\mathbf{w}_e, \mathbf{s}_e) \equiv D_{\mathbf{w}}F_e - D_{\mathbf{s}}F_e\,(D_{\mathbf{s}}G_e)^{-1}(D_{\mathbf{w}}G_e)\,. \tag{B.4}$$

The linear stability properties of an equilibrium point to the DAE system is determined by the eigenvalues of $\mathcal{Q}$.

Proposition B.1. *The DAE equilibrium is linearly stable when all the eigenvalues z of $\mathcal{Q}$ satisfy* $\mathrm{Re}(z) < 0$.

The entries of $\mathcal{Q}$ consist of partial derivatives of $\mathbf{F}$ and $\mathbf{G}$, which we can approximate by finite differences. With this numerical approach, the stability criterion was implemented in §4.2 and §4.3 for identifying two and three-spot steady-state configurations in the unit square that are linearly stable for the DAE dynamics (2.30).